JOURNAL OF GEOPHYSICAL RESEARCH: EARTH SURFACE, VOL. 118, 2105–2123, doi:10.1002/jgrf.20127, 2013

Impact of flow routing on catchment area calculations, slope estimates, and numerical simulations of landscape development

Eitan Shelef[1] and George E. Hilley[1]

Received 15 January 2013; revised 12 July 2013; accepted 9 August 2013; published 11 October 2013.

[1] Flow routing across real or modeled topography determines the modeled discharge and wetness index and thus plays a central role in predicting surface lowering rate, runoff generation, likelihood of slope failure, and transition from hillslope to channel forming processes. In this contribution, we compare commonly used flow-routing rules as well as a new routing rule, to commonly used benchmarks. We also compare results for different routing rules using Airborne Laser Swath Mapping (ALSM) topography to explore the impact of different flow-routing schemes on inferring the generation of saturation overland flow and the transition between hillslope to channel forming processes, as well as on location of saturation overland flow. Finally, we examined the impact of flow-routing and slope-calculation rules on modeled topography produced by Geomorphic Transport Law (GTL)-based simulations. We found that different rules produce substantive differences in the structure of the modeled topography and flow patterns over ALSM data. Our results highlight the impact of flow-routing and slope-calculation rules on modeled topography, as well as on calculated geomorphic metrics across real landscapes. As such, studies that use a variety of routing rules to analyze and simulate topography are necessary to determine those aspects that most strongly depend on a chosen routing rule.

Citation: Shelef, E., and G. E. Hilley (2013), Impact of flow routing on catchment area calculations, slope estimates, and numerical simulations of landscape development, *J. Geophys. Res. Earth Surf.*, *118*, 2105–2123, doi:10.1002/jgrf.20127.

1. Introduction

[2] The routing of mass across landscapes underlies many hydrological and geomorphological models [*Fairfield and Leymarie*, 1991; *Tarboton*, 1997; *Zhou and Liu*, 2002]. These models rely on drainage-area-based metrics such as Total Drainage Area (TDA), and Specific Catchment Area (SCA) to infer variables such as channel discharge, surface lowering rate, generation of overland flow, the dominance of diffusive versus advective processes that shape the landscape, and the likelihood of slope failure [*Montgomery and Dietrich*, 1994; *Refsgaard*, 1997; *Perron et al.*, 2008, 2009; *Tucker and Hancock*, 2010]. The widespread availability of Digital Elevation Models (DEMs) has led to the development of algorithms that route flows over digital representations of a landscape and determine the drainage area at each point [e.g., *O'Callaghan and Mark*, 1984; *Freeman*, 1991; *Fairfield and Leymarie*, 1991; *Quinn et al.*, 1991; *Lea*, 1992; *Costa-Cabral and Burges*, 1994; *Tarboton*, 1997; *Orlandini et al.*, 2003; *Qin et al.*, 2007; *Orlandini and Moretti*, 2009]. In these flow-routing rules, the complexity of overland flow processes is typically simplified by assuming steady uniform flow and neglecting inertial and pressure effects, so that flow is driven exclusively by gravity. Such algorithms are particularly amenable to operation over regularly gridded topography, where elevations are sampled at equally spaced nodes on a rectangular grid.

[3] While desirable for many reasons [e.g., *Qin et al.*, 2007] the rectangular grid representation of topography poses challenges to flow routing because the orthogonal grid direction may be imprinted on the flow's pathway. This problem motivated the development of various grid-based routing rules that attempt to balance efficiency, simplicity, and accuracy in routing flows and calculating basin areas. Nonetheless, most rules are geometrically inconsistent in that they describe flows as one-dimensional in planview [*Costa-Cabral and Burges*, 1994; *Moore and Grayson*, 1991; *Chirico et al.*, 2005], which is an undesirable outcome of flow routing into diagonal elements that attempt to reduce the grid imprint on flow pathways. We attempt to rectify some of these flow-routing issues by presenting a new routing rule that operates over a triangular representation of the gridded data to minimize the impact of the grid. We then compare outcomes of various flow-routing rules using standard geometric tests that are modified to capture the accuracy of drainage area calculations produced by individual flows. We also compare the impact of different flow-routing and slope-calculation rules on predicted locations of geomorphologic process transitions and slope failure

Additional supporting information may be found in the online version of this article.

[1]Department of Geological and Environmental Sciences, Stanford University, Stanford, California, USA.

Corresponding author: E. Shelef, Department of Geological and Environmental Sciences, Stanford University, Stanford, CA, 94305 USA. (shelef@stanford.edu)

2169-9003/13/10.1002/jgrf.20127

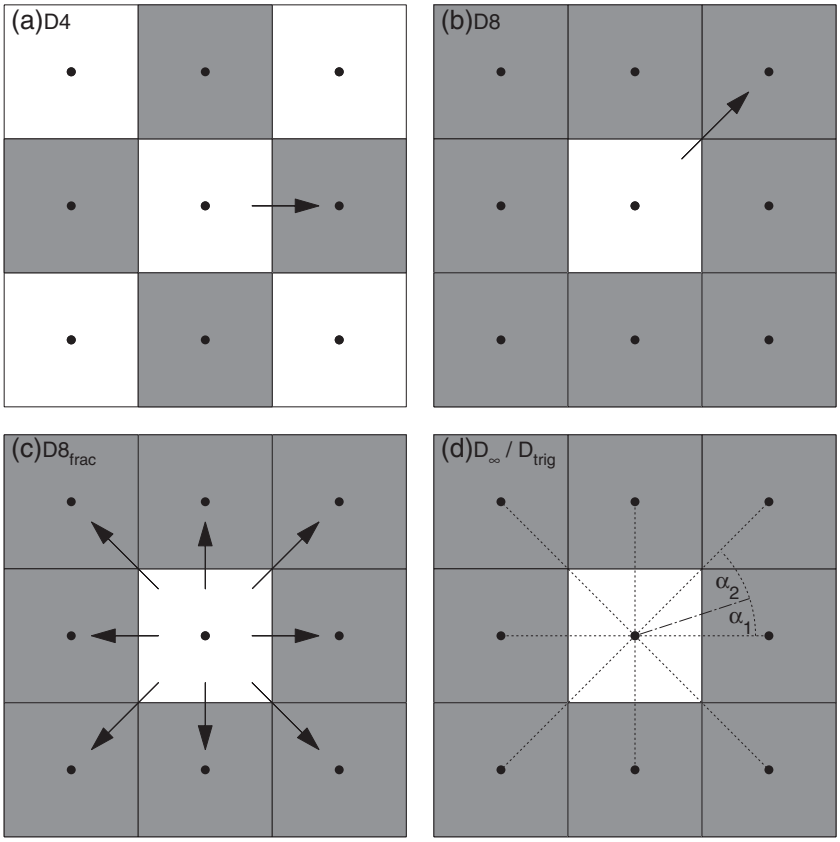

Figure 1. Different flow-routing rules applied over a nine-cell kernel. In this example the elevation of the central node is the highest in the kernel, gray-filled elements are those into which flow can be routed, and arrows point toward the elements into which flow is routed. (a) $D4$ rule: Flow is routed into the steepest-descent cell of the four orthogonal cells (i.e., five-cell kernel). (b) $D8$ rule: Flow is routed into the steepest-descent cell of the eight surrounding cells. (c) $D8_{\text{frac}}$ rule: Flow is routed into all downslope cells, where the slope to each cell determines the flow partitioning. (d) D_∞: Flow is routed into one or two cells that are downslope of the steepest-descent triangular facet. α_1 and α_2 are the angles used for flow partitioning by D_∞, and the line separating them is oriented in the direction of the facet's gradient.

occurrence over high resolution ALSM topography. Finally, we examine the effect of different flow-routing and slope-calculation rules on the outcomes of landscape evolution models. We found that these rules leave a significant impact, both visually and statistically, on numerically simulated surfaces and on analysis of ALSM topography. Thus, studies investigating those landscape metrics that are sensitive to a chosen flow-routing rule will be necessary to determine robust measures of landscape attributes.

2. Methods

2.1. Flow Routing

2.1.1. Common Routing Rules

[4] Flow-routing rules typically distribute the drainage area of a given grid element into a set of neighboring elements according to some prescribed rule. This rule typically uses node-to-node slopes to determine the fraction of the area that is partitioned to each surrounding downslope element. Flow-routing rules are divided into Single and Multiple Flow Direction rules (SFD and MFD, respectively), which partition flow into one (SFD) or many (MFD) surrounding cells. We consider four common rules for partitioning flow ($D4, D8, D_\infty$, and $D8_{\text{frac}}$ i.e., the MFD method of *Freeman* [1991]) when evaluating the impact of flow-routing rules on catchment area calculations and synthetic topography produced through numerical simulations.

[5] $D4$ is a five-cell kernel method that routes flow to one of the four cardinal directions based on the steepest descent (Figure 1a). This method favors convergent flows along paths aligned with the cardinal grid directions. These undesired artifacts were somewhat rectified with the development of the $D8$ rule [*O'Callaghan and Mark*, 1984], in which flows are routed into the steepest of the eight neighboring downslope cells (Figure 1b). In this case, slopes to diagonal cells are scaled to account for the longer flow path in these directions. As with $D4$, $D8$ favors convergent flow, since no flow is distributed between multiple surrounding cells [*Freeman*, 1991; *Quinn et al.*, 1991; *Tarboton*, 1997].

[6] In an attempt to disperse flow across divergent topography, *Freeman* [1991] proposed a nine-cell-kernel MFD routing rule (hereby referred to as $D8_{\text{frac}}$, Figure 1c) that partitions flow into all downslope cells based on their slopes, according to the rule

$$F_i = \frac{S_i^p}{\sum_{i=1}^{N} S_i^p}, \tag{1}$$

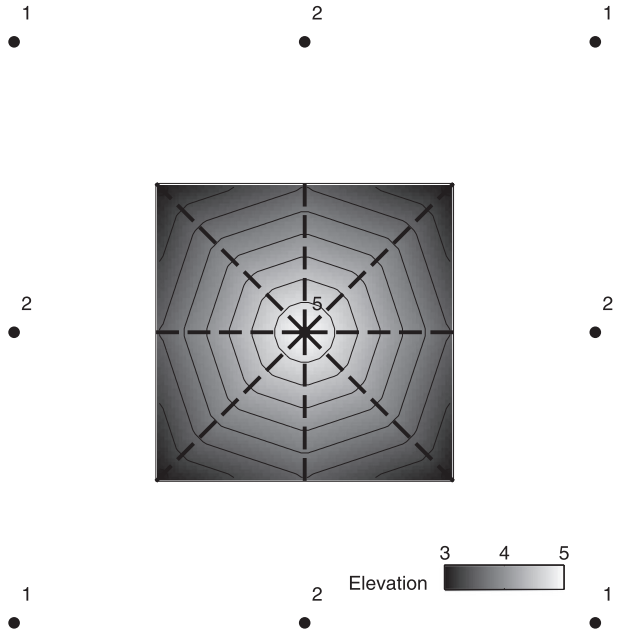

Figure 2. Illustration of D_{trig}'s subelement topography formed by eight triangular facets defined by the nine-cell-kernel nodes (black circles). The node's elevation values are printed in black next to each node. Facet boundaries are marked by dashed lines. Note that the surface extent is limited to the central cell only so that the only node within this domain is the element-centered node. Contours and color scale illustrate the elevation variations within the element, the rounding of contours adjacent to facet's boundaries is an artifact of the contouring algorithm.

where F_i is the fraction of the area routed from a node to the ith surrounding node, N is the number of downslope cells, S is the slope from the central node to the ith surrounding node, and p is a prescribed calibration parameter. $p > 1$ values favor flow routing into relatively steep surrounding elements while $p < 1$ preferentially partitions flow into relatively shallower surrounding elements. Freeman found that $p = 1.1$ produced SCA values closest to those expected for known, simple topographic forms.

[7] *Tarboton* [1997] developed the D_∞ rule, a nine-cell-kernel steepest-descent MFD rule that distributes flow into one or two elements based on the gradient of the steepest of eight triangular facets defined by a node and its surrounding eight neighbors. Each facet is anchored at the central, and two of the eight neighboring nodes (Figure 1d). The gradient vector of the steepest of these facets is used to divide the flow between the outer nodes of this facet according to the angles (α_1, α_2, Figure 1d) between this gradient vector and the facet's bounding legs. In Figure 1d, for example, the fraction of the central cell drainage area that is partitioned to the node to its right is $\frac{\alpha_1}{\alpha_1+\alpha_2}$. This allows flow to be partitioned to two surrounding cells in the case that the gradient orientation does not align with one of the facet's bounding legs.

2.1.2. New Flow-Routing Rule

[8] We propose a new flow-routing rule, D_{trig}, that allows flow to be distributed among multiple downslope grid-cells, while honoring the two-dimensional plan-view geometry of flows by partitioning them only along orthogonal grid directions. To accomplish this, we decompose the topography into a set of triangular facets, whose extent is defined only within their associated grid cell (Figure 2), but their gradient is defined based on adjacent grid nodes according to the D_∞ rule of *Tarboton* [1997]. Rather than asserting that the steepest descent facet dictates flow partitioning, D_{trig} explicitly describes the internal topography of a grid-cell using a set of eight triangular facets (Figure 2), and partitions flow between these facets and those associated with neighboring grid-cells. In doing so, D_{trig} routes flow across the facet's and grid-cell's edges rather than through corners. This is achieved in two consecutive stages: (1) The topography is decomposed into a set of triangular facets for which the gradient and mean elevation are calculated (this is done after pits in the original DEM are filled). (2) The facets are then ordered by their mean elevation and the drainage area is progressively added and partitioned from upslope facets to those progressively lower according to the rule described below. A record is kept when area is partitioned into facets across grid-cells so that the drainage area associated with cells on the orthogonal grid is also progressively calculated (see pseudocode in the supporting information).

[9] To partition flow between facets, we first define a coordinate system for each triangular facet such that the central node of a nine-cell kernel lies along one of the acute angles of the isosceles triangular facet, while nodes located along the cardinal and diagonal grid directions form the right and acute angles of the facet, respectively. The two orthogonal legs of the facet define our coordinate directions labeled $\hat{i}$ and $\hat{j}$ in Figure 3a. The location of the central node is denoted (x_0, y_0, z_0), the node allocated along the $\hat{i}$ direction is (x_1, y_1, z_1), and the diagonal node is located at (x_2, y_2, z_2). Given this geometry, the facet slope in the $\hat{i}$ and $\hat{j}$, directions are

$$g_{\hat{i}} = \frac{z_0 - z_1}{x_1 - x_0}, \qquad g_{\hat{j}} = \frac{z_1 - z_2}{y_2 - y_1}, \tag{2}$$

and the facet's gradient vector is $\vec{g} = [g_{\hat{i}}, g_{\hat{j}}]$. Because each of the surrounding nodes defines an independent set of triangular facets, the facet for each central node extends along the $\hat{i}$ direction from (x_0, y_0, z_0) to $(\frac{x_0+x_1}{2}, y_0, \frac{z_0+z_1}{2})$ and along the $\hat{j}$ direction from $(\frac{x_0+x_1}{2}, y_0, \frac{z_0+z_1}{2})$ to $(\frac{x_0+x_1}{2}, \frac{y_0+y_2}{2}, \frac{z_0+z_2}{2})$, as represented by the gray facet in Figure 3a. As such, the mean elevation of this facet is $\bar{z} = (4z_0 + z_1 + z_2)/6$. Next, flow is partitioned from each facet into surrounding facets by intersecting a line orientated parallel to $\vec{g}$ with the node of the facet that allows this line to traverse the facet's area (Figure 3). If $\vec{g}$ points toward this node, the intersecting line delineates the facet's drainage divide, and area is partitioned between the neighboring facets according to the subareas defined by this drainage divide (Figures 3b, 3c). In contrast, when $\vec{g}$ plunges away from the node, the entire area of the facet is partitioned through the leg of the triangle opposite to this node into the adjoining facet (Figures 3d, 3e).

[10] The cumulative area for each facet is calculated by partitioning flow from the facets with the highest mean elevation into those that are progressively lower. In the context of routing between grid cells, the conversion from facet-based to grid cell-based cumulative area can be computed by summing all the areas partitioned into a grid cell by facets

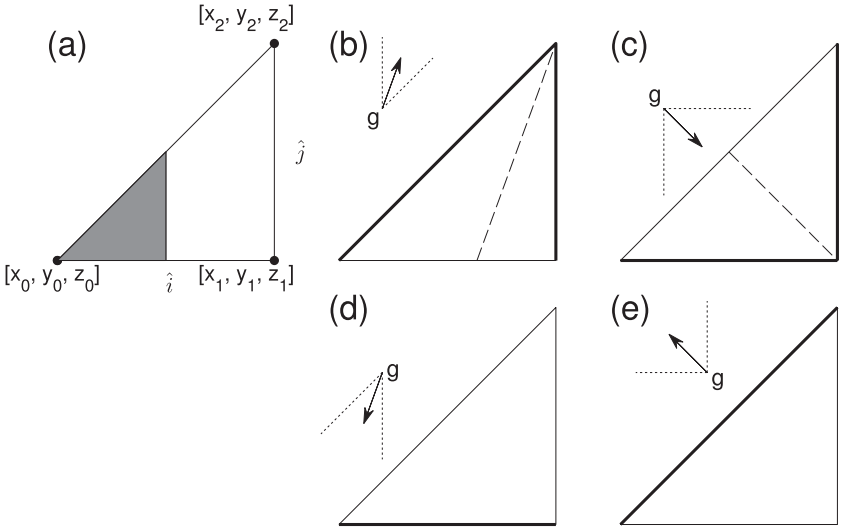

Figure 3. Examples of flow partitioning from a triangular facet. (a) A triangular facet, the local coordinates, and the $\hat{i}$, $\hat{j}$ directions. (b) The case where the line oriented in the direction of $\vec{g}$ intersects node $[x_2, y_2, z_2]$ and is plunging toward the node. The dashed lines that bound $\vec{g}$ mark the range of orientations where $\vec{g}$ intersects this node and divides the area of the facet into two triangles. In this case, the facet's drainage area is partitioned proportionally to the area of each of the triangles bounded between the facet's drainage divide (i.e., the dashed intersecting line) and the facet's bounding legs. The area is partitioned into the two facets sharing the bold colored facet legs. (c) Same as Figure 3b, except that $\vec{g}$ is dipping toward node $[x_1, y_1, z_1]$. (d) Same as Figure 3b except that $\vec{g}$ is plunging away from node $[x_2, y_2, z_2]$. (e) Same as Figure 3d, except that $\vec{g}$ is plunging away from node $[x_1, y_1, z_1]$.

of neighboring cells. This results in routing through only the orthogonal boundaries of the grid cells; hence, it eliminates the need to distribute flow directly to diagonal nodes in a DEM.

[11] Special cases of opposing flow between facets, or of flat facets, arise in rare configurations of node elevations (these rare configurations occur in < 0.001 of all grid nodes for the natural and modeled landscapes analyzed). In these cases, the drainage area of a facet is partitioned into the lowest of the surrounding facets. Special cases of returning flows, in which the subgrid resolution of the facets allows them to be routed into and out of grid elements multiple times, may over estimate an element's drainage area. While such cases did not occur in the analyses we ran, we algorithmically addressed their potential occurrence by tracking and identifying these cases and subtracting their area contribution when calculating the area of each cell on the regular grid.

2.2. Comparative Tests for Flow-Routing Rules

[12] Flow-routing rules are traditionally tested over synthetic surfaces where the Total Drainage Area (TDA), and Specific Catchment Area (SCA) can be calculated analytically. Typically, outward cones, inward cones, and tilted planes [*O'Callaghan and Mark*, 1984; *Freeman*, 1991; *Fairfield and Leymarie*, 1991; *Quinn et al.*, 1991; *Lea*, 1992; *Costa-Cabral and Burges*, 1994; *Qin et al.*, 2007; *Tarboton*, 1997] are used for this purpose, although other configurations are used in some cases [*Zhou and Liu*, 2002; *Freeman*, 1991; *Qin et al.*, 2007]. For the flow-routing rules, the TDA is simply the area that was routed into a grid cell, and the SCA is this area divided by the flow width (subjectively defined here as Δx for all routing schemes). The analytical calculations typically assume that each point in the landscape contributes equally to drainage area, so that the SCA equals $\frac{r}{2}$ for an outward cone, and $\frac{(r_o^2 - r^2)}{2r}$ for an inward cone, where r is the radius at the point of interest and r_o is the radius of the outer extent of the cone.

[13] We found that standardly used benchmarks that assume equal area contribution for each element in the landscape may offset errors in drainage area sourcing some points with errors from other points (Figure 4). To detect such errors, we modified these benchmarks to analyze the performance of flow-routing rules when considering point sources. When applied over nonplanar surfaces (e.g., cones), such modified benchmarks can also detect a dependence between the performance of a flow-routing rule and the orientation of the topographic gradient. In the case of the outward facing cone, this was accomplished using a finite contributing area source ($\mathrm{d}A$) as a radial element defined by the angular and radial intervals $\mathrm{d}\theta$ and $\mathrm{d}r$, respectively (Figure 5). The SCA of areas downslope of $\mathrm{d}A$ is thus $\frac{1}{r}\frac{\mathrm{d}A}{\mathrm{d}\theta}$. This was compared with the SCA computed by different flow-routing rules and different point source orientations to evaluate the rule's local accuracy. This comparison was quantified using the Root Mean Squared (RMS) error of the difference between SCA produced by each flow-routing method, and that expected theoretically at each point in the discretized benchmark. The discordance between the geometry of cylindrical elements used in the SCA analytical calculation and the rectangular elements used in numerical flow routing can introduce errors into SCA estimates. We calculated SCA at radial distance > 60 grid elements to compare analytical and numerical SCA estimates. At this radial pixel distance the cylindrical elements are nearly

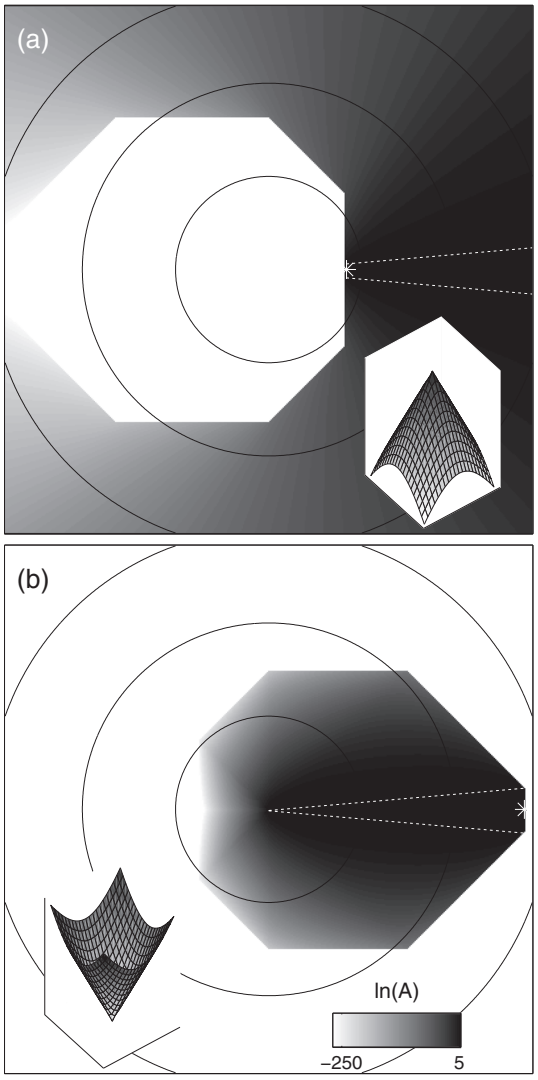

Figure 4. (a) Natural log of drainage area (Δx^2) calculated with $D8_{frac}$ over an outward facing cone. The contributing area is sourced at a 10° wide point source centered around the white asterisk. Dotted white lines mark the theoretical boundaries of the influence zone for this point source. (b) Same as Figure 4a, but only over inward facing cone. Inset figures show the surface topography of these inward and outward facing cones. Note the dispersion of flow beyond the theoretical influence zone of the source (dotted white lines)—when flow-routing rules are benchmarked using the standard method where all elements have equal area contribution, dispersion errors from multiple upslope elements may offset each other so the overall calculated SCA appears similar to the analytically based expectation. Note the log-scale color scheme used to highlight the extent of flow dispersion.

equidimensional and within 2% of the dimensions of rectangular elements.

[14] We visually compared flow partitioning patterns over natural surfaces by calculating flow routing from a single grid element over a 100 × 100, 2 m resolution ALSM DEM from the Eel River basin in Northern California Coast Range, where several ALSM based studies were conducted [e.g., *Passalacqua et al.*, 2010; *Mackey and Roering*, 2011; *DeLong et al.*, 2012]. Additionally, we explored the impact of flow routing on the spatial transition from advective (e.g., channel forming) to diffusive (e.g., soil creep) dominated portions of the landscape. To do so, we prescribed equal area contribution to all grid elements and calculated the Péclet number (*Pe*) for each grid element [*Perron et al.*, 2008, 2009, 2012]:

$$Pe = \frac{K(3A)^{m+1/2}}{D}, \tag{3}$$

where K is the bedrock erodibility coefficient, A is the drainage area, m is the area scaling exponent for the detachment limited erosion rule, and D is the soil diffusion coefficient.

[15] We also explored the impact of different routing rules on process thresholds determined by both slope and drainage area. To do so, we compared the spatial distribution of grid elements dominated by overland flow processes (when all elements have the same area contribution), using the steady state hydrologic model of *Dietrich et al.* [1992] and *Montgomery and Dietrich* [1994]:

$$\frac{A}{b} \geq \frac{T}{q} \sin\beta, \tag{4}$$

where b is the unit length of the contour across which the catchment is draining (here we use $b = \Delta x$), T is the soil transmissivity, q is precipitation rate, and β is the slope angle associated with each grid element and calculated as $\beta = \tan^{-1} S$, where S is the element's slope whose computation is described in section 2.3.

2.3. Landscape Development Models

[16] Geomorphic Transport Law (GTL)-based landscape development models often use rules that parameterize

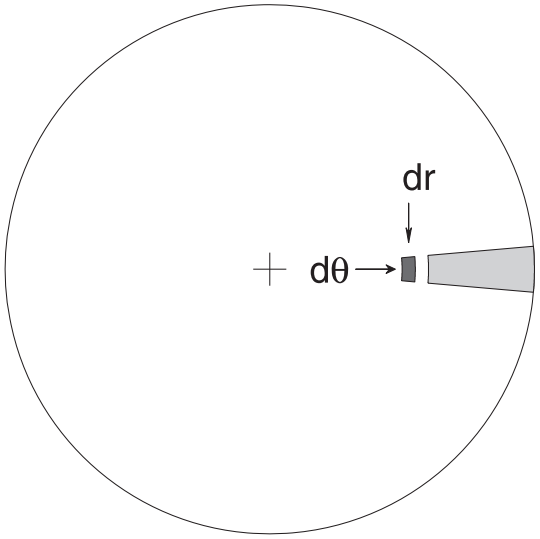

Figure 5. Illustration of a proposed source distribution that reveals local errors in flow-routing rules applied to downslope elements. The contributing drainage area dA (dark gray), starts at a radius of $r = r_{min}$, extends over a radius interval dr, and spans an angle interval dθ. The influence zone used for comparison starts slightly downslope from r_{min} + dr (light gray).

surface lowering or sediment transport rate in terms of catchment area. Thus, the choice of flow-routing rules may affect the evolution of synthetic landscapes. We studied the impact of the $D4, D8, D8_{\text{frac}}$, and D_{trig} routing rules on the time-invariant form of landscapes simulated using GTLs. We uplift the model domain at a constant rate (U) and lower it by detachment-limited stream incision [*Howard and Kerby*, 1983; *Seidl and Dietrich*, 1992; *Howard*, 1994; *Whipple and Tucker*, 1999] and soil diffusion [*Howard*, 1994; *Culling*, 1960, 1963, 1965]:

$$\frac{\mathrm{d}z}{\mathrm{d}t} = U - (KA^m|\nabla z_c|^n - D\nabla^2 z), \tag{5}$$

where the left and right terms in the parentheses represent the combined effect of advective stream incision and diffusive soil creep, respectively [*Howard*, 1994; *Tucker and Bras*, 1998; *Dietrich et al.*, 2003; *Perron et al.*, 2008]. In equation (5), K is the bedrock erodibility coefficient, A is the drainage area (here calculated after all pits are filled), m and n are exponents, ∇z_c is the channel slope, D is the soil diffusion coefficient, and $\nabla^2 z$ is the Laplacian operator applied to the surface. The model integrates equation (5) using an 8–9 order explicit, time step adaptive, Runge-Kutta integration algorithm that ensures error control [*Dormand and Prince*, 1980; *Press et al.*, 2007]. All models share the same grid size ($Nx = 100, Ny = 100$) and dimensions ($\Delta x = \Delta y = 5$ m), initial and boundary conditions (periodic along the right and left boundaries, and constant elevation boundaries along the top and bottom boundaries), and model duration (6 Myr). Model parameters were set to the following: $U = 1 \times 10^{-4}$ m yr^{-1}, $K = 2 \times 10^{-5}$ m^{1-2m} yr^{-1}, $m = 0.5$, $n = 1$, and $D = 1.4 \times 10^{-3}$ m^2 yr^{-1}.

[17] ∇z_c is calculated downslope in the direction of flow, and thus the flow-routing rule and the channel slope are linked. For $D8$ and $D4$, ∇z_c is calculated using the elevation of each cell (z_i) and the elevation of the cell into which flow is routed (z_{i+1}) as

$$|\nabla z_c| = \frac{z_i - z_{i+1}}{\Delta l}, \tag{6}$$

where $\Delta l = \Delta x, \Delta l = \sqrt{2}\Delta x$ for orthogonal and diagonal directions, respectively. For $D8_{\text{frac}}$, ∇z_c is computed using a weighted mean slope:

$$|\nabla z_c| = \frac{1}{N}\sum_{i=1}^{N} S_i^p, \tag{7}$$

where S is calculated in the manner described by equation (6). For D_{trig}, we calculate ∇z_c as

$$|\nabla z_c| = \sqrt{\bar{S_x}^2 + \bar{S_y}^2}, \tag{8}$$

where $\bar{S_x}$ and $\bar{S_y}$ are the slopes in the x and y directions, respectively, that are averaged over all downslope-facing facets. For D_∞, we use $|\nabla z_c| = |\vec{g}|$, where $|\vec{g}|$ is the slope of the facet of steepest descent.

2.3.1. Comparing Landscapes Modeled by Different Slope and Routing Rules

[18] We compare steady state elevations between pairs of simulated landscapes using the correlation coefficient:

$$C_c = \frac{\sum_{i=1}^{N_t}({}^1z_i - {}^1\bar{z}_i) \times ({}^2z_i - {}^2\bar{z}_i)}{\sqrt{\sum_{i=1}^{N_t}({}^1z_i - {}^1\bar{z}_i)^2} \times \sqrt{\sum_{i=1}^{N_t}({}^2z_i - {}^2\bar{z}_i)^2}}, \tag{9}$$

where ${}^1z_i$ and ${}^2z_i$ are the ith elevation of the last time step of the two models compared, ${}^1\bar{z}_i$ and ${}^2\bar{z}_i$ are the mean elevations of these two models, and N_t is the total number of elevation nodes in each model. C_c equals 1 and –1 for perfect correlation and anticorrelation, respectively, and approaches zero for no correspondence between the two models. In addition to comparing elevations throughout the steady state model domain, we compared the distribution of channel segment lengths and orientations. Segments were identified in the models by computing the Strahler order of each node in the modeled topography (Strahler order for models produced by MFD schemes was calculated with $D8$) and extracting paths bounded by junctions with channels of Strahler order ≥ 2. Lengths of these segments (l) were calculated by tracking flow between these junctions while orientations were calculated as the mean orientation of the segment. We then calculated the modulus of the orientation with respect to 90° (γ) to measure the deviation of channel orientation from the grid-imprinted orthogonal directions. Differences in the distributions of these values between the four linked routing and slope configurations were measured using a Kruskal-Wallis test (K-W test, *Kruskal and Wallis* [1952]) the failure of which suggests that at least one of the observed distributions was drawn from a distinct distribution. Finally, to investigate the decoupled influence of the slope and routing rules on the resulting landscapes, we extract parameters of interest from the γ, l, and elevation values of each of the 16 modeled landscapes produced by all possible area and slope rule combinations (i.e., four slope rules times four routing rules). We then evaluate the impact of the flow-routing and slope-calculation factors with a two-way ANOVA test over these parameters of interest (each parameter has 16 values, one for each of the 16 models), where each of these two factors has four groups corresponding to the four routing and slope rules we used (i.e., $D4, D8, D8_{\text{frac}}$, and D_{trig}). Failure of this test indicates distinct group means, and suggests that the factor/s for which the test failed significantly affect/s the variance in the parameter of interest.

3. Results

3.1. Benchmark Tests

3.1.1. Flow Divergence Benchmark (Outward Facing Cone)

[19] Figure 6 shows SCA values for a flow divergence benchmark over an outward facing cone for the section of the cone bounded between $80\Delta x < r < 195\Delta x$. For this benchmark, $\mathrm{d}A$ is defined by $\theta = 10°$, and $\mathrm{d}r = 10\Delta x$ starting at a distance $r = 60\Delta x$ from the cone center. The cone slope is $\mathrm{d}z/\mathrm{d}r = -1$ and the area into which $\mathrm{d}A$ drains, hereafter termed the influence zone, was compared with theoretical values starting at distance of $10\Delta x$ downslope of $\mathrm{d}A$. This comparison was conducted for cases in which the 10° angular interval was centered at orientations of 0°, 23°, 45° from east. Results illustrate that $D4$ and $D8$ tended to focus on one or two flow paths depending on the angular location of $\mathrm{d}A$, and show the imprint of the cardinal and diagonal grid directions. The SCA values calculated using $D_\infty, D8_{\text{frac}}$, and D_{trig} underestimate the true SCA within the theoretical influence zone. The SCA values for D_∞ and $D8_{\text{frac}}$ decrease more rapidly with r than those calculated analytically and with

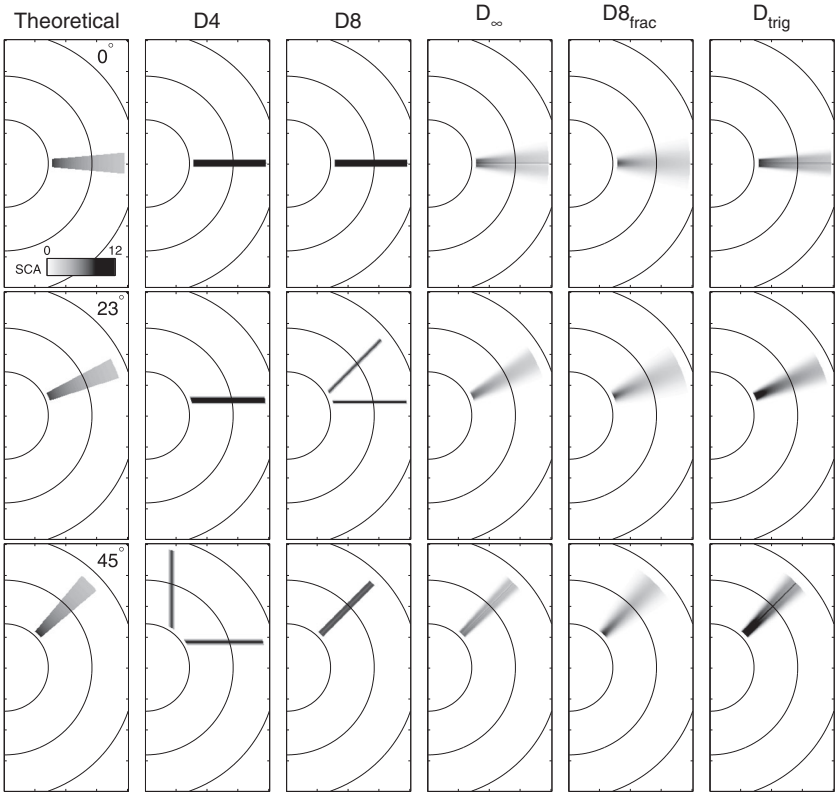

Figure 6. Plots of SCA (Δx) associated with different flow-routing rules (noted at the top of each column of subfigures) for flows starting at different locations along an outward facing cone of 401×401 elements. Each row of figures shows results for a 10°, $10\Delta x$ long source area, centered at the angle specified in the leftmost plot of each row.

D_{trig}. RMS values show that D_{trig} performs comparably to D_{∞} and $D8_{\text{frac}}$, and that these three methods produce lower RMS values than $D4$ and $D8$ (Figure 7, first column).

3.1.2. Flow Convergence Benchmark (Inward Facing Cone)

[20] Figure 8 shows the SCA values for a flow convergence benchmark consisting of an inward facing cone for the section of the cone bounded between $60\Delta x < r < 175\Delta x$. For this benchmark, $\mathrm{d}A$ is bounded by an angle of $\theta = 10°$, and radial interval of $\mathrm{d}r = 10\Delta x$ starting at a distance of $185\Delta x$ from the cone center. The cone slope is $\mathrm{d}z/\mathrm{d}r = 1$. We compared SCA between routing methods and theory within a zone that starts $10\Delta x$ downslope of $\mathrm{d}A$. As with the outward cone, this test was conducted for cases in which the 10° angular interval is centered at orientations of $0°, 23°, 45°$ from east. Results illustrate that $D4$ tends to inhibit flow convergence until flow paths reach an angle of 45° from the cone center. $D8$ lacks flow convergence along the 45° direction, and converges rapidly down the cone's slope along the 23° direction. SCA values of D_{∞}, $D8_{\text{frac}}$, and D_{trig} show continuously convergent patterns similar to that of the analytical SCA, with D_{∞} and $D8_{\text{frac}}$ slightly underestimating, and D_{trig} overestimating the true SCA. When $\mathrm{d}A$ is oriented 0°, $D8_{\text{frac}}$ is more dispersive then the analytical SCA. RMS values show that D_{trig} performs comparably to D_{∞} and $D8_{\text{frac}}$, and that these three methods perform better than $D4$ and $D8$ (Figure 7, second column).

3.1.3. Flow Direction Benchmark (Tilted Plane)

[21] Figure 9 shows the SCA values for a flow direction benchmark over a plane of unity slope tilted $0°, 23°, 45°$ toward east. For this benchmark $\mathrm{d}A$ is 40 cells wide, and extends nine to 13 cells downslope. RMS values show that all routing rules perform flawlessly except for $D8_{\text{frac}}$ (Figure 7, third column, first row) when plane is tilted 0° to the east. For a plane tilted 23°, the imprint of the cardinal and diagonal grid directions is apparent for $D8$ and $D4$, while other rules perform comparably better. For a plane tilted 45°, the imprint of the orthogonal grid directions is apparent for $D4$ (Figure 7, third column).

3.2. Flow Across Natural Landscapes

[22] Figure 10 illustrates flow routing produced by different rules over a DEM located within the Eel River basin. In this case, flow is sourced from a single grid element. The log scaling of catchment area in this figure highlights differences between SFD and MFD routing rules. SFD rules produce flows that traverse a single-thread set of downslope elements, while MFD rules distribute flows between adjacent elements. Downslope of the source element, $D4$ routes area along a linear segment, while $D8$ allows flow to traverse the topography in a way that more closely approximates downslope flow (Figures 10a, 10b). While most rules route flow only within the watershed of the source element, $D8_{\text{frac}}$ can partition flow across drainage divides so that a

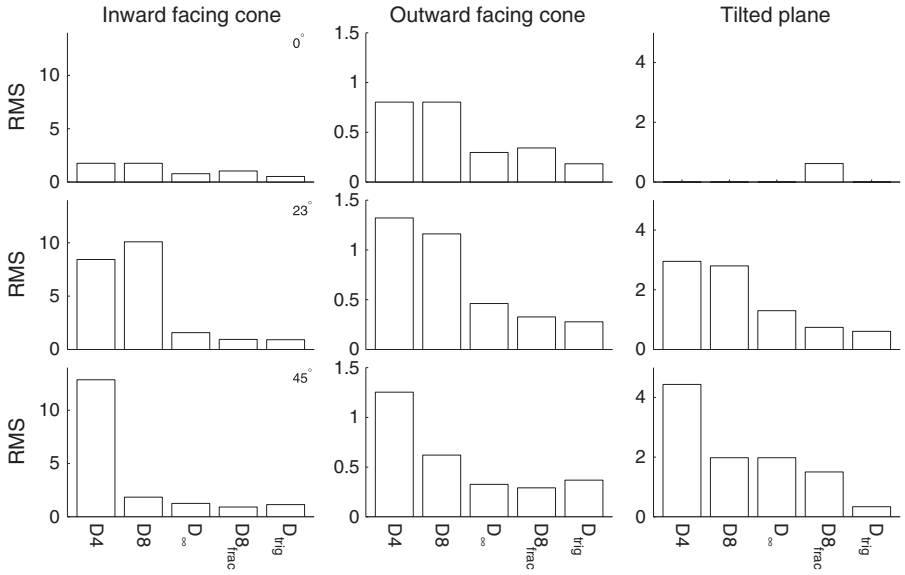

Figure 7. Bar plots of the RMS values of the difference between the analytically calculated SCA and that of the different flow-routing rules (noted at the top of each column of subfigures). RMS values are based on the SCA values shown in Figures 6, 8, and 9. The angle specified in the leftmost plot of each row indicates the orientation of the source area (for cones, first and second columns) or the tilt direction (for a plane, third column).

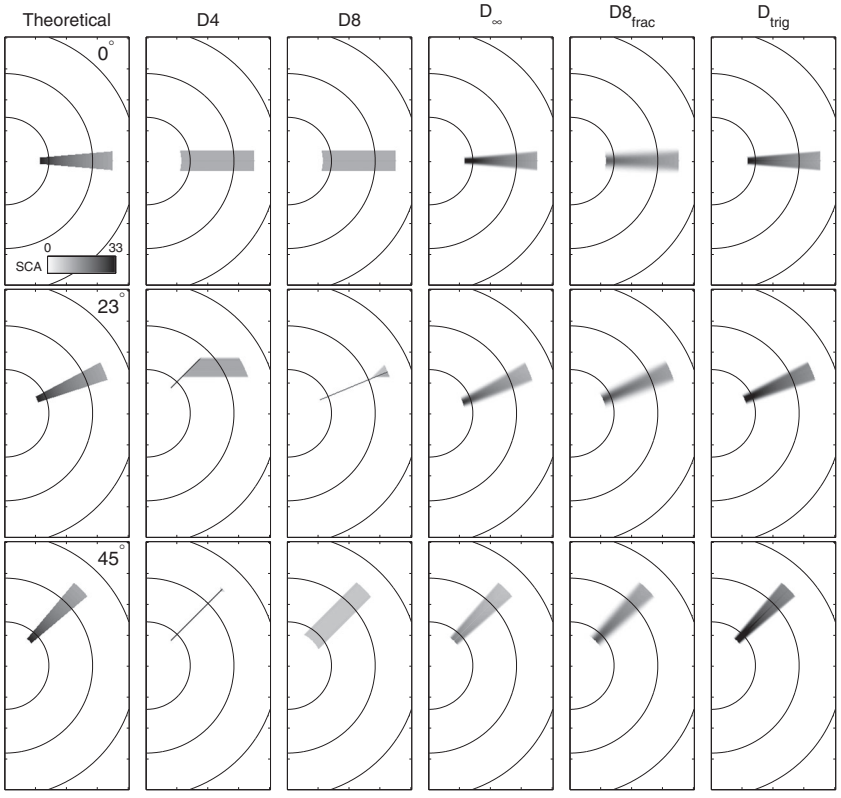

Figure 8. Plots of SCA associated with different flow-routing rules (noted at the top of each column of subfigures) for flows starting at different locations along an inward facing cone of 401×401 elements. Each row of figures shows results for a 10°, $10\Delta x$ long source area, centered at the angle specified in the leftmost plot of each row.

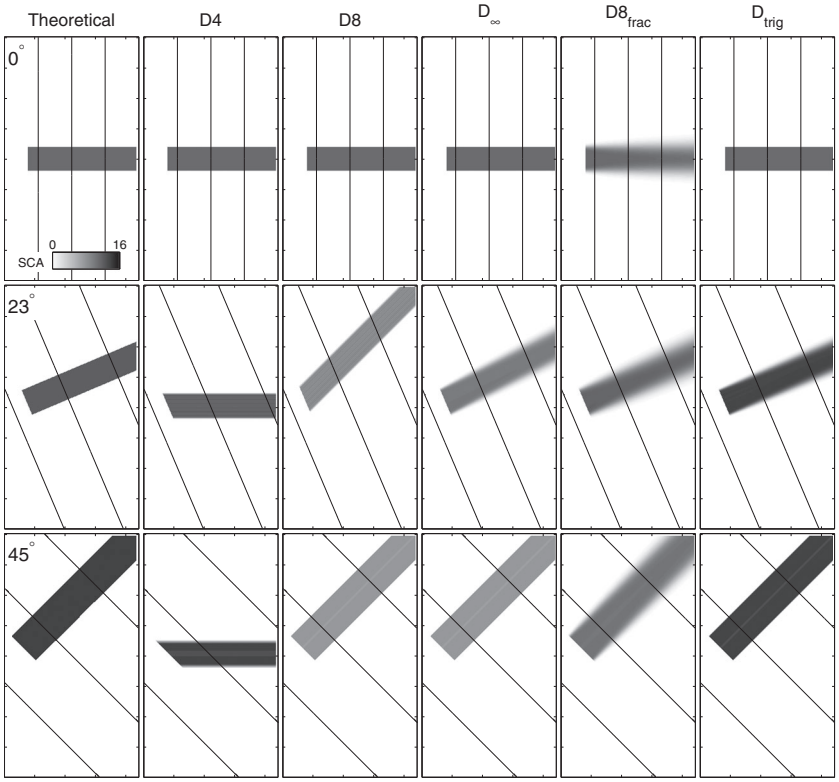

Figure 9. Plots of SCA associated with different flow-routing rules (noted at the top of each column of subfigures) for flows starting at different locations along a titled plane of 401 × 401 elements. Each row of figures shows results for a 39 to 40 Δx-wide, nine to 13 Δx-long, source area over a plane tilted at the angle specified to the left of the row.

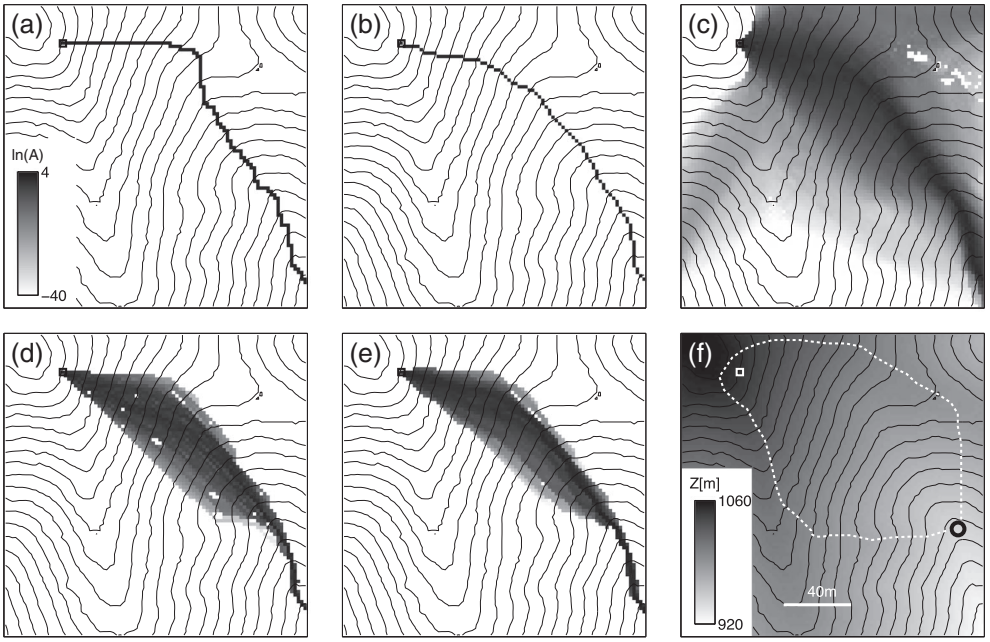

Figure 10. Plots showing the influence zone of a single grid element (marked by a square) over small drainages in the Eel River basin. Element area is 2 × 2 m and contour spacing is 6 m. (a) $D4$, (b) $D8$, (c) $D8_{\mathrm{frac}}$, (d) D_{∞}, (e) D_{trig}, and (f) elevation values, scale, and delineated divide of an arbitrary element downslope of the source element (dashed white line). Note the log-scale color scheme used to highlight the differences in drainage area between routing rules.

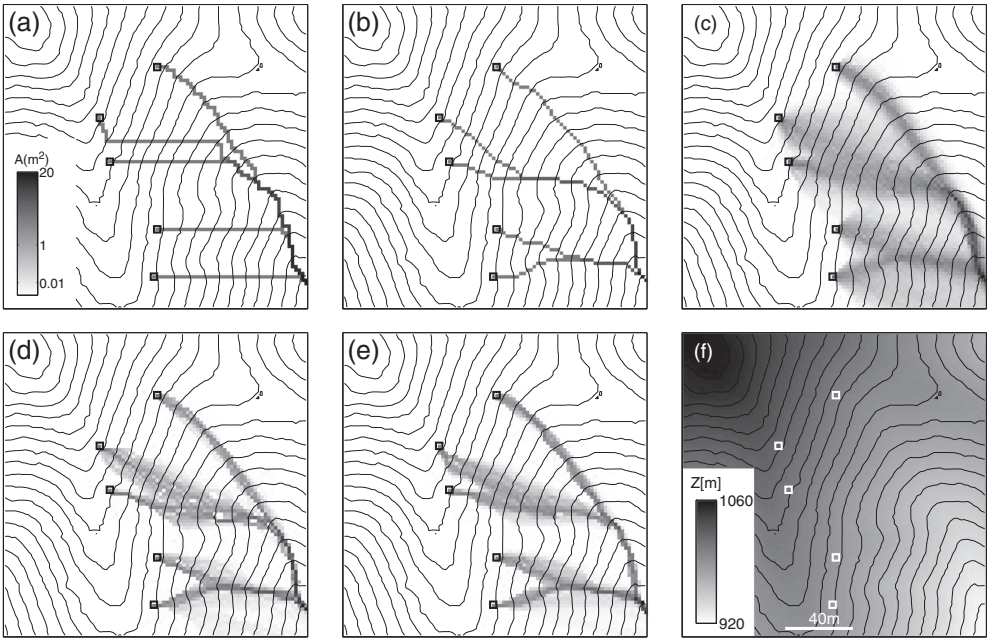

Figure 11. Plots showing the influence zones of five grid elements (marked by squares) over a small drainage in the Eel River basin. Element area is 2 × 2 m and contour spacing is 6 m. (a) $D4$, (b) $D8$, (c) $D8_{\mathrm{frac}}$, (d) D_{∞}, (e) D_{trig} and (f) elevation values and scale.

fraction of the source element drainage area is routed into neighboring basins (Figure 10c). D_{∞} and D_{trig} behave similarly to one another; however, the flow partitioned by D_{∞} occupies a slightly larger influence zone than that of D_{trig}. The influence zone of D_{∞} contains more points of zero contributing area in between areas where flow has been routed relative to D_{trig}. This likely results from the fact that D_{∞} routes area to only one of the eight facets, which produces more convergent individual flow paths relative to D_{trig} (Figures 10d, 10e).

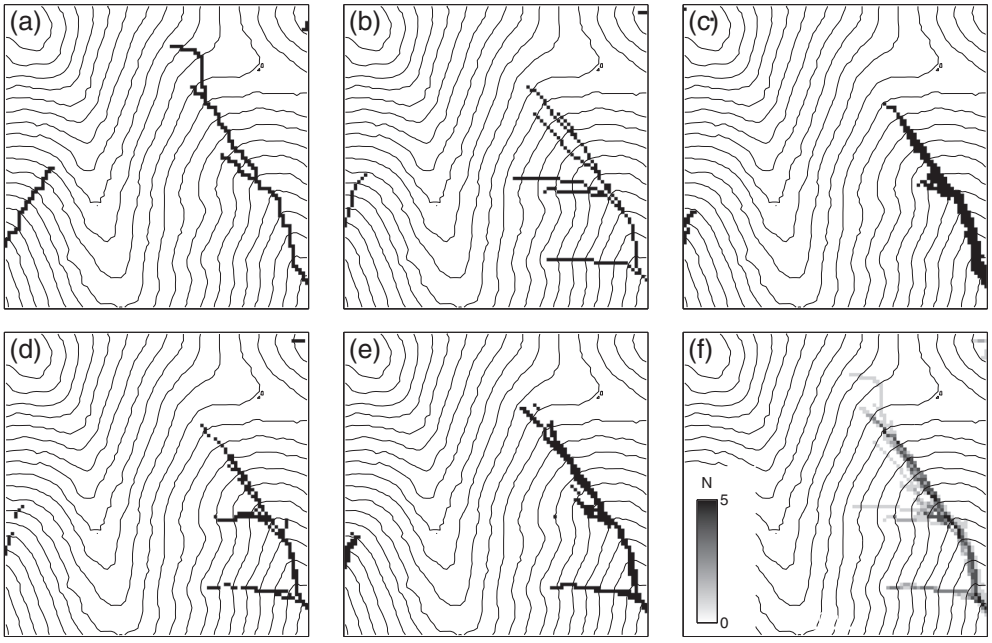

Figure 12. Plots showing grid elements in which $Pe > 1$ for $K/D = 3.3 \times 10^{-4}$ m^{-2} plotted over contoured ALSM data for the various routing rules where area is sourced from all grid elements. (a) $D4$, (b) $D8$, (c) $D8_{\mathrm{frac}}$, (d) D_{∞}, (e) D_{trig}, and (f) super-position of all $Pe > 1$ elements detected by the different routing schemes. Elements are colored by the number of routing schemes that predict $Pe > 1$ within a particular grid element. Note the correspondence between areas of $Pe > 1$ and the zones of convergence in Figure 11.

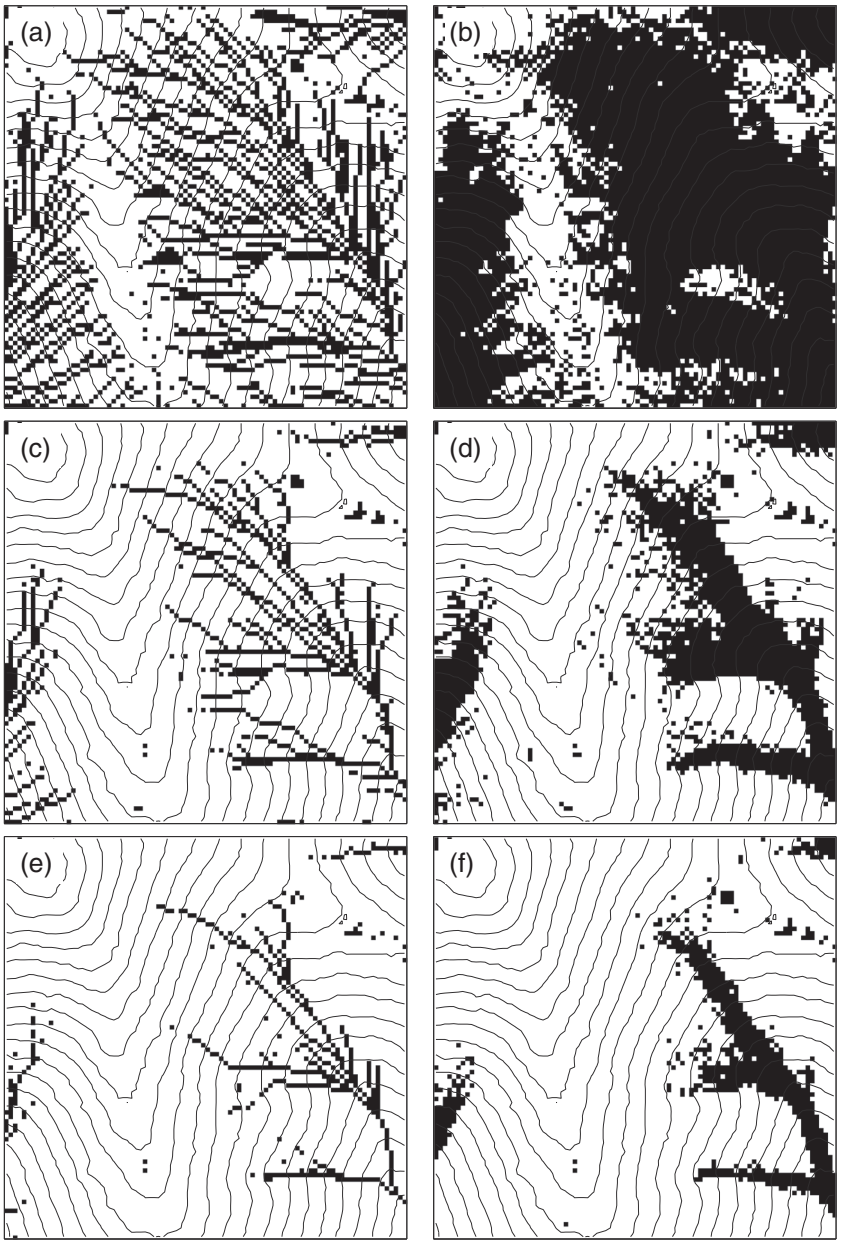

Figure 13. Plots showing grid elements associated with saturation overland flow (i.e., $\frac{A}{b} \geq \frac{T}{q} \sin\beta$) over contoured ALSM data for (a, c, e) $D8$ and (b,d,f) $D8_{\text{frac}}$ and for various values of $\frac{T}{q}$. (Figures 13a, 13b) $\frac{T}{q}$ = 60 m, (Figures 13c, 13d) $\frac{T}{q}$ = 240 m, and (Figures 13e, 13f) $\frac{T}{q}$ = 540 m. Note that area is sourced from all grid elements.

[23] Figure 11 shows the influence zone of five single-element sources over the same DEM as in Figure 10. The strong imprint of grid directions characteristic of $D4$ (Figure 11a) results in parallel flows and inhibited flow convergence relative to $D8$ (Figure 11b) and the MFD schemes (Figures 11c–11e). $D8_{\text{frac}}$ is associated with wider influence zone whose points have low drainage area (Figure 11c) compared to those of D_{∞} and D_{trig} (Figures 11d, 11e, respectively).

[24] We analyzed the influence of flow-routing rules on the calculated extent of advective (e.g., convergent channelization) versus diffusive (e.g., dispersive hillslope creep) processes within the Eel River DEM. To do this, we calculated the Péclet number (equation (3)) over the DEM shown in Figures 10 and 11 using a prescribed $\frac{K}{D}$ ratio (3.3×10^{-4} m^{-2}) and m value (0.5), where A is computed with different flow-routing rules. We show points in the landscape at which $Pe > 1$ in Figure 12 for each of the flow-routing rules. The reduced flow convergence produced by $D4$ restricts $Pe > 1$ to only large valleys in this area (Figures 12a, 11a). $D8$ ameliorates this situation somewhat, allowing advective processes to dominate in convergent areas that are farther upslope relative to $D4$ (Figures 12b, 11b). Small, upslope tributaries in which advective processes are expected to dominate are also absent when using $D8_{\text{frac}}$ (Figure 12c) due to the dispersion associated with it

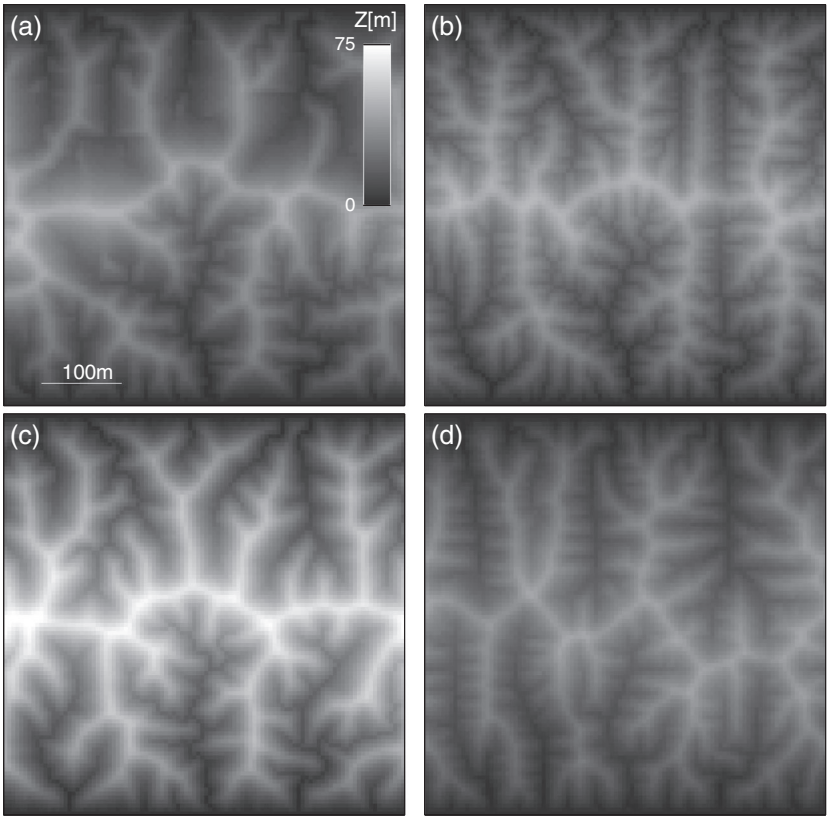

Figure 14. Synthetic, steady state DEMs produced by models using the following sets of slope and routing rules: (a) $D4$, (b) $D8$, (c) $D8_{\mathrm{frac}}$, and (d) D_{trig}.

(Figures 4, 11c). However, the reduced dispersion of D_∞ and D_{trig} allows $Pe > 1$ to exist in upslope, convergent portions of the landscape (Figures 12d, 12e, 11d, 11e). In general, MFD methods allow isolated areas of the landscape to have $Pe > 1$ because of the fact that flows can disperse and reconverge downslope depending on the local topography (Figures 11c–11e).

[25] Differences in dispersion and convergence of flows produced by different flow-routing methods likely affects predictions of the extent of Saturation Overland Flow (SOF) in landscapes using a steady state hydrologic model [*Dietrich et al.*, 1992, 1993]. To study the impact of routing rules on the predicted extent of SOF, we calculated catchment area across the DEM shown in Figure 10, and used this value with equation (4) to determine points in the landscape where SOF is expected to operate (Figures 13, S1). We compare two end-member routing rules; ($D8$; Figure 13 a, c, and e, and $D8_{\mathrm{frac}}$; Figure 13 b, d, and f) using values of $T/q = 60$ m (Figure 13 a,b), 240 m (Figure 13 c, d), and 540 m (Figure 13 e, f). The convergence associated with $D8$ is reflected by the presence of individual flow-paths along which SOF is expected to be generated. In contrast, broad areas of convergence are expected to generate SOF in the case of $D8_{\mathrm{frac}}$. In general, areas of SOF extend to higher areas of the landscape when using $D8$ because flow is concentrated along individual flow paths, rather than being dispersed across broad areas as is the case for the MFD methods. The existence of isolated elements of overland flow for $D8$ is due to the inclusion of slope in equation (4), so that elements of low slope and high drainage area may generate overland flow. The extent of landsliding within the landscape shows a similar sensitivity to the routing and slope rules, because the local slope and the extent of subsurface saturation exerts an important control on the distribution of landsliding in landscapes (e.g., *Dietrich et al.* [1992]; *Montgomery and Dietrich* [1994]; see Figure S2).

3.3. Synthetic Landscapes

[26] Flow-routing and slope-calculation rules determine catchment area and channel slopes, which serve as inputs to GTL-based models of landscape development. Thus, we expect that the choice of flow-routing and slope-calculation rules may impact the topographic attributes of simulated topography. We explored these impacts on simulated landscapes by integrating equation (5) for a period of time that is required to reach a steady state topography in which $dz/dt = 0$ at each point in the model domain [e.g., *Howard*, 1994]. Identical initial conditions, which consisted of a single realization of random noise, were used for all simulations. This steady state condition provided a set of topographies that can be directly compared between flow-routing rules.

[27] Figure 14 shows steady state landscapes generated by a GTL-based landscape development model based on equation (5). The models differ in that the value of A and ∇z_c in equation (5) are calculated with different sets of flow-routing and slope-calculation rules.

3.3.1. Topography

[28] We observed differences in the relief and channel patterns within synthetic landscapes produced using different flow-routing and slope-calculation rules for identical

Table 1. Cross-Correlation Values Between Pairs of Modeled Landscapes Shown in Figure 14

	$D4$	$D8$	$D8_{frac}$	D_{trig}
$D4$	1.000	0.730	0.787	0.706
$D8$		1.000	0.853	0.724
$D8_{frac}$			1.000	0.703
D_{trig}				1.000

initial and boundary conditions (Figure 14). $D8_{frac}$ produced a higher relief landscape than other rules. Landscapes produced by $D8_{frac}$ and $D4$ appear less dissected than those produced by D_{trig} and $D8$. Orthogonal channel directions are visually more prevalent for landscapes produced by $D4$ and D_{trig}.

[29] We compared elevation values at each point within the modeled landscape using the cross-correlation values (C_c; equation (9), results reported in Table 1) between landscapes generated using four different flow-routing rules. All C_c values were higher than 0.7, with values associated with comparisons with D_{trig} being relatively low. The lowest correlation was between the surfaces produced by $D8_{frac}$ and D_{trig}, and the highest one is for those produced by $D8_{frac}$ and $D8$.

3.3.2. Channel Metrics

[30] Comparison of elevation values may not capture differences in the geometry of channel networks. To quantify differences in simulated channel geometries, we measured the deviation of channel orientations from the grid imprinted orthogonal directions (γ), and report their cumulative distribution functions (CDFs) in Figure 15. All landscapes share a step in the CDF at $\gamma \simeq 0°$, indicating that many segments are oriented N-S or E-W (parallel or perpendicular to the model's constant elevation boundary conditions). The fraction of $\gamma \simeq 0°$ is larger for D_{trig}, which is consistent with visual inspection of the modeled landscapes. A large step at $\gamma \simeq 45°$ is apparent in the CDFs of both $D8_{frac}$ and $D8$, indicating that these rules are associated with a high number of diagonally oriented segments. The differences between these distributions are statistically significant based on a K-W test (p-value = 1.4×10^{-2}).

[31] Differences in downslope flow convergence between the flow-routing rules may cause the length of individual channel segments to differ between flow-routing methods. We explored this effect by calculating CDFs of the length of individual channel segments (l) in each of the simulated landscapes (Figure 16). Segment length is generally longer for $D4$ compared to other rules. The l distributions are statistically different based on a K-W test (p-value = 1.5×10^{-8}).

[32] In the simulated landscapes, the flow-routing and slope-calculation rules influence the resulting topography. We explored the relative and absolute impact of these rules on the model outcomes by creating simulations that used the 16 possible combinations of the four flow-routing and slope-calculation rules (Figure S3). The modeled topography produced by each of these 16 simulations was then used to extract and examine CDFs of l and γ, (Figures S4, S5). To further explore the influence of the flow-routing and slope-calculation factors on different geomorphologic variables, we used two-way ANOVA tests for these two factors

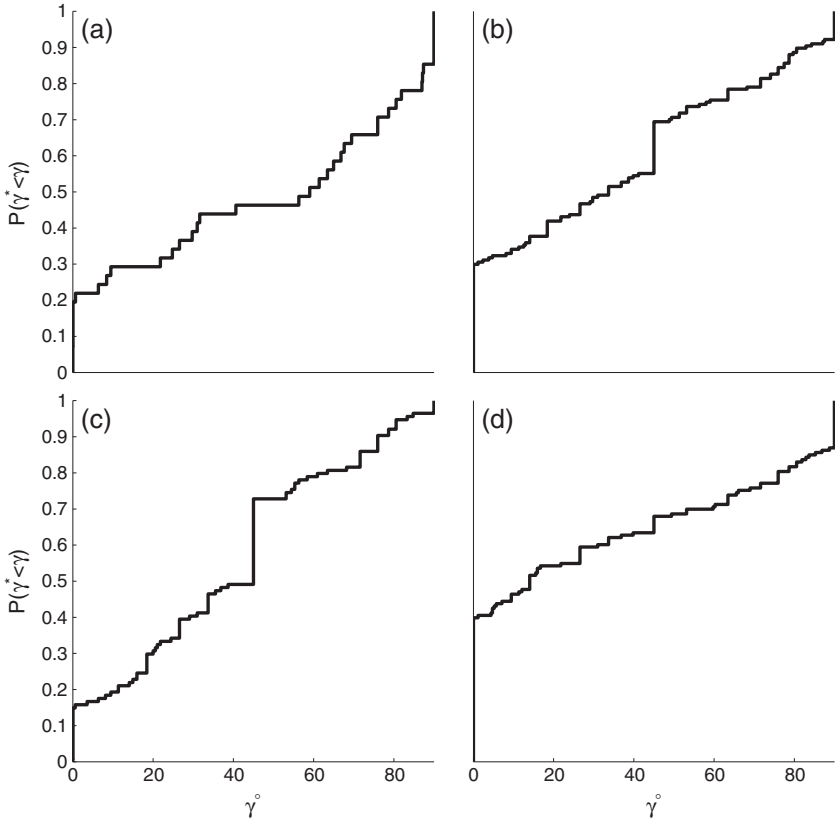

Figure 15. CDFs of the modulus of segment orientation relative to 90° (γ) for modeled landscapes shown in Figure 14. (a) $D4$, (b) $D8$, (c) $D8_{frac}$, and (d) D_{trig}.

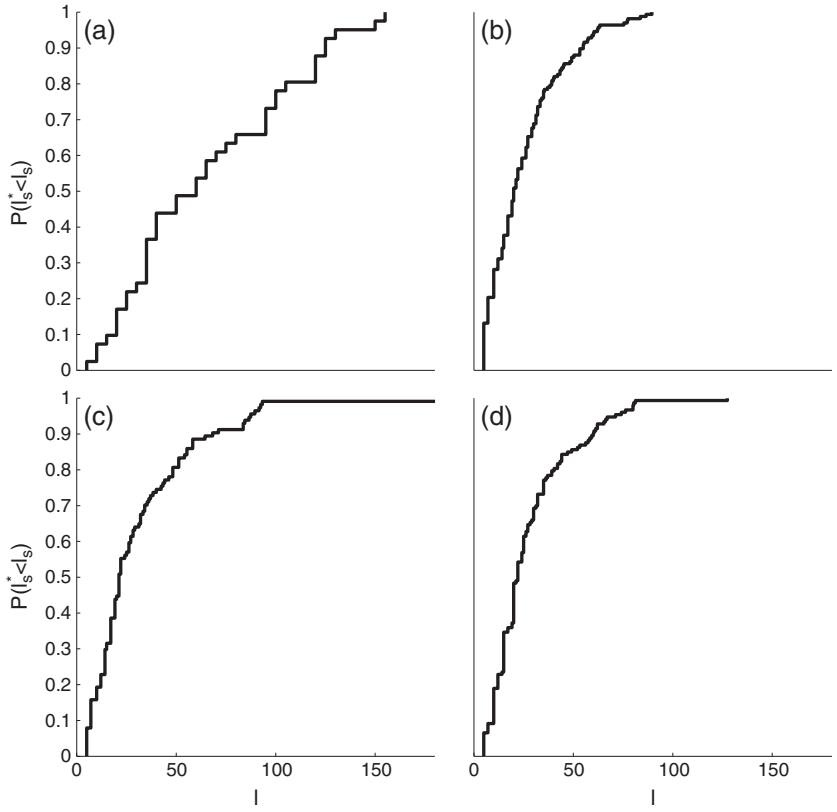

Figure 16. CDFs of segments length (l) for modeled landscapes shown in Figure 14. (a) $D4$, (b) $D8$, (c) $D8_{\text{frac}}$, and (d) D_{trig}.

over the following variables: (a) median segment length, (b) mean segment length, (c) the Poisson parameter (λ) that best fits the Poisson-like segment-length distribution, (d) the fraction ($N_{\gamma 45}$) of diagonally oriented segments (i.e., $44° \leq \gamma \leq 46$) out of all γ measurements, (e) the fraction ($N_{\gamma 90}$) of orthogonally oriented segments (i.e., $89° \leq \gamma \leq 90° \bigcup 0° \leq \gamma \leq 1°$) out of all γ measurements, and (f) the topographic relief. For the segment length variables (i.e., mean and median segment length and λ), the ANOVA test rejected the null hypothesis (i.e., H_0: there is no difference between mean segment lengths across models, $\alpha = 0.05$, Table 2, rows 1–3) for the flow-routing factor, and failed to reject it for the slope-calculation factor. This suggests that these segment length variables are influenced mostly by the flow-routing rule, and that this influence is statistically significant. For the flow orientation variables (i.e., $N_{\gamma 45}$, $N_{\gamma 90}$), however, the test rejected the null hypothesis ($\alpha = 0.05$, Table 2, rows 4, 5) for both slope-calculation and flow-routing factors, where the p-values for the slope-calculation factor are an order-of-magnitude lower than those for the flow-routing factor. These results suggest that both flow-routing and slope-calculation rules have significant impact on these segment orientation variables, and that the impact of the slope-calculation rule is greater than that of the flow-routing rule. Finally, we applied the test to the topographic relief of the modeled landscape. Results show that the null hypotheses can be rejected for the slope-calculation factor ($\alpha = 0.05$, Table 2, row 6), but cannot be rejected for the flow-routing factor. Hence, the slope-calculation rule significantly impacts topographic relief and has higher influence on the relief than the flow-routing rule.

4. Discussion

4.1. Advantages and Limitations of D_{trig}

[33] D_{trig} attempts to route flows in a manner that balances efficiency, simplicity, and accuracy, while reducing the imprint of the orthogonal grid directions. In decomposing the grid into $n \times 8$ triangular facets, D_{trig} achieves a more realistic description of the routing process at the expanse of increased complexity and computational burden. This method explicitly depicts interelement topography

Table 2. Statistics of Flow-Routing and Slope-Calculation Rules Impact on Modeled Landscape Geometry[a]

Geomorphic Parameters	Slope Calculation	Flow Routing
Median segment length	1.5×10^{-1}	5.8×10^{-7}
Mean segment length	4.4×10^{-1}	1.1×10^{-5}
λ	2.4×10^{-1}	1.4×10^{-4}
$N_{\gamma 45}$	3×10^{-3}	1.3×10^{-2}
$N_{\gamma 90}$	8×10^{-3}	4×10^{-2}
Topographic relief	5.2×10^{-1}	4×10^{-2}

[a] P-values produced by a two-way ANOVA test that explores the influence of flow-routing and slope-calculation rules on various geomorphic parameters. λ is the Poisson distribution parameter, $N_{\gamma 45}$ and $N_{\gamma 90}$ are the fractions of γ values that are within 1° from diagonal and orthogonal orientations, respectively.

(Figure 2), and partitions flow through edges, rather than corners, based on a facet's drainage divide (Figure 3). D_{trig} enables flow divergence that is common over convex portions of the landscape [*Freeman*, 1991; *Fairfield and Leymarie*, 1991; *Quinn et al.*, 1991], produces flow patterns that capture transitions from divergent to convergent topography (Figure 10), and circumvents the need to route flows through cell corners [e.g., *Costa-Cabral and Burges*, 1994; *Moore and Grayson*, 1991, Figure 3]. Although D_{trig} is advantageous for these reasons, it nonetheless contains artifacts that arise from the grid decomposition into facets. For example, D_{trig} partitions area between facets by assuming that all the incoming area is distributed homogeneously within the facet. In reality, area that enters the facet on one side of the facet's drainage divide should not be distributed across this divide. Addressing such shortcomings will increase memory usage and computational requirements and reduce efficiency and simplicity (such as in the case of the DEAMON routing rule [*Costa-Cabral and Burges*, 1994; *Tarboton*, 1997]). Nonetheless, comparison benchmarks show that such problems do not crop up at a frequency that greatly degrades the rule's performance, as our study shows that it performs comparably to other MFD routing rules.

[34] The choice of a slope-calculation rule is influenced by two potentially exclusive factors; its linkage with a flow-routing rule and the spatial alignment between a grid node and the slope associated with it. For example, the slopes associated with steepest descent routing-rules (i.e., $D4, D8, D_{\infty}$, section 2.3), are defined midway between the cell-centered node, and the steepest descent node (or nodes, in the case of D_{∞}), and hence may be inadequate to describe the slope at the cell-centered node where equations (5) and (4) are applied. This misalignment between the slope and node locations can be resolved with a central-difference slope rule, where the slope at a node is calculated from the elevation difference between nodes on its opposite sides [*Perron et al.*, 2008; *Burrough and McDonnell*, 1998]. However, a central-difference rule disentangles the linkage between the slope and routing rules, and may introduce artifacts such as assigning slope values to nodes located at the bottom of asymmetric topographic depressions. The slope-averaging rules such as those used for D_{trig} and $D8_{\text{frac}}$ (e.g., equation (7)) at least maintain the linkage between a slope and a routing rule.

[35] Choices related to implementation of flow-routing rules attempt to balance physical realism with simplicity and efficiency. This sometimes creates situations in which basic flow geometry or physics is violated at the expense of simplicity and efficiency. For example, $D4, D8$, and in many cases D_{∞}, route flows into a single downslope surrounding cell, whereas in reality, flow dispersion is an inevitable component of all natural flows. Even when flow is routed into all downslope elements, such as with $D8_{\text{frac}}$, the partitioning of flow between downslope elements according to their slope is an arbitrary choice underlain by the assumption that the arrangement of the cell's internal divides is related to those slopes. These arbitrary assumptions require ad hoc fixes to reproduce benchmarks: in the case of $D8_{\text{frac}}$, the slope weighting exponent is set to $p = 1.1$, which was calibrated by *Freeman* [1991] based on comparison with particular benchmarks. While D_{trig} eliminates some of these arbitrary choices by explicitly defining the internal topography of an element and its internal divides, as described above, there are a number of ad hoc choices that we made to reduce the computational burden of this method. Thus, while D_{trig} performs in a similar way to many of the other flow-routing rules, it probably contains an increment more of physical realism than other flow-routing rules.

4.2. Benchmarks

[36] The SCA and RMS values calculated for the different flow-routing rules are directly affected by the definition of flow width. For nine-cell-kernel methods, the definition of flow width is ambiguous for both MFD and SFD rules, because they imply zero flow width when routing flows through cell's corners [*Costa-Cabral and Burges*, 1994; *Moore and Grayson*, 1991; *Chirico et al.*, 2005]. This leads to subjectivity in the definitions of flow width [*Chirico et al.*, 2005], where flow-width values range between $0.354\Delta x$ [*Quinn et al.*, 1991] and $\sqrt{2}\Delta x$ [*Costa-Cabral and Burges*, 1994; *Chirico et al.*, 2005], and may depend on flow orientation, grid resolution, and the specific rule used [*Chirico et al.*, 2005]. In light of this ambiguity, our subjective choice of a constant flow width for all cases (Δx) is within the typical range used, ensures simplicity and consistency between rules, and is consistent with previous studies that use nine-cell-kernel methods [*Zhang and Montgomery*, 1994; *Wolock and G. McCabe Jr*, 1995; *Chirico et al.*, 2005].

[37] Benchmark tests show that the geometry of the grid strongly influences the path of routed flows for the $D4$ and $D8$ rules (Figures 6, 8, 9). In the former case, routing shows strong preference for the orthogonal directions of the grid, while a secondary diagonal preference was observed for the latter rule (Figures 6, 8). In all cases, the performance of the flow-routing rule varies according to the orientation of the surface relative to the point source (Figures 6–9), suggesting that the routing rule may interact with complex natural topographies in ways that may be difficult to anticipate in advance. Additionally, differences in relative RMS values for different surface orientations suggest that the choice of the best-performing routing rule may depend on the local orientation of the surface.

[38] Differences in the relative performance of flow-routing rules also arose when the extent of the source area was varied. In particular, the performance of $D8_{\text{frac}}$ improves relative to other rules as source area dimensions increase because errors in the distribution of individually generated flows combine to offset one another in a way that reduces the overall RMS for the standard benchmark tests. This is clearly seen when calculating RMS for different angular spans of the source area for the cone benchmark tests (Figure 17); as $\mathrm{d}\theta$ increases, the RMS calculated using $D8_{\text{frac}}$ systematically decreases relative to the other routing rules. Thus, the apparent success of this method may depend on the empirical calibration of p (equation (1)) to the large $\mathrm{d}\theta$ benchmarks used by *Freeman* [1991]. Whether or not $D8_{\text{frac}}$ performs better than the uncalibrated methods over complex real surfaces is unclear, but $D8_{\text{frac}}$'s improper routing of individual flows across real topographies (Figure 10) suggests that it may not. Flow dispersion produced by $D8_{\text{frac}}$ is larger than that expected theoretically. We found that overestimation of dispersion is also produced by D_{trig} and D_{∞} (Figure S6). Importantly, our results suggest that new flow-routing rules should be benchmarked against both cumulative SCA

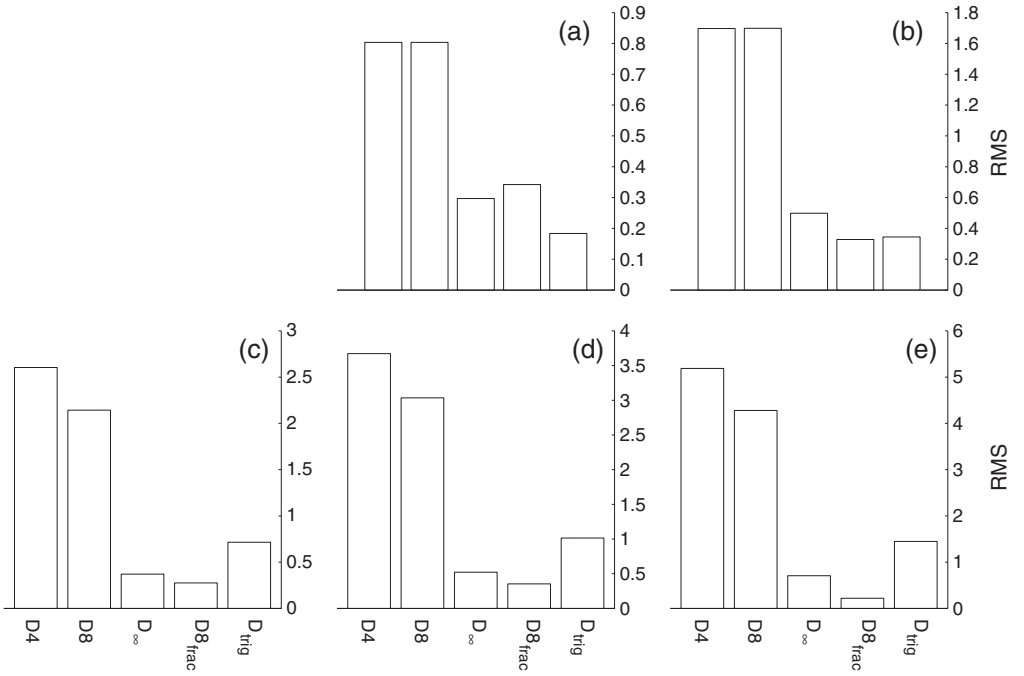

Figure 17. RMS for varying angular span (dθ) for a point source centered at 0° from east over an outward facing cone. (a) dθ=10°, (b) dθ=45°, (c) dθ=90°, (d) dθ=180°, (e) dθ=360°. Note the varying ratios between the RMS values of the different routing schemes. In particular, note the relative decrease in the RMS of $D8_{\text{frac}}$ as the angular span increases.

calculated using a uniform source distribution, as well as benchmarks that generate flows at a point source to assess a method's performance.

4.3. Analysis of Real Landscapes

[39] Our analysis reveals that the choice of flow-routing rule plays an important role in the calculation of catchment area, inference of SOF across landscapes, and the predicted distribution of landslides within real topography. This effect is especially pronounced in the upland, low-catchment-area portions of the landscape. The choice of a routing rule for the analysis of channel systems may depend on the specific attributes of the digital topographic data being analyzed, and the objectives of a particular study. For example, MFD rules such as D_{trig} and D_{∞} may capture downslope changes in channel width, depict zones of subchannel divergence and convergence (Figures 10d, 10e), and aid in relating spatial variations in channel geometry to variables such as slope and drainage area when analyzing high-resolution topographic data in which channels in the landscape are much wider than the DEM resolution (i.e., pixel size). SFD rules, on the other hand, will reduce channels to single-thread features and fail to capture the full extent of the active channel and surrounding floodplains (Figures 10a, 10b). On the other hand, SFD rules are likely to provide a better description of the channel network and its properties compared to MFD rules when the channel is much narrower than the DEM resolution. In this case, MFD rules may overestimate channel width and portray unrealistic internal channel geometry.

[40] Inappropriate choice of a flow-routing rule is not the only error source in hydrologic analysis over DEMs. For example, drainage area computation is also sensitive to errors in landscape elevation that stem from the acquisition and processing involved in DEMs production. When landscape slopes are low with respect to elevation errors, these errors may cause routing inaccuracies that may exceed those that stem from an inappropriate choice of a flow-routing rule.

[41] In analyzing channel networks, MFD rules obfuscate measurement of some channel metrics. Measuring flow length, for example, is ambiguous in these schemes because of the nonuniqueness of the flow path from a particular source to its downslope destination. This introduces difficulties in calculating length-dependent parameters such as sinuosity or Péclet number. Further, the recursive algorithms that are commonly used in defining drainage extent over DEMs [*Band*, 1986; *McCormack et al.*, 1993] are greatly complicated when conducted with MFD schemes, and may lead to unrealistic outcomes for schemes such as $D8_{\text{frac}}$, which can route flow across drainage divides (Figure 10c).

[42] We found that routing rules may have significant impact on the analysis of process transitions across DEMs. In particular, the way in which flow is routed over hillslopes affects the delineation of areas dominated by fluvial processes. The topographic transition between a divergent hillslope and a convergent channel is reflected by D_{trig} and D_{∞} as a shift from dispersive to convergent flows (Figures 10d, 10e). In contrast, this transition is not reflected by the single thread channels produced by $D4$ and $D8$ (Figures 10a, 10b), and is masked by $D8_{\text{frac}}$ because of its tendency to disperse flow broadly across landscapes (Figure 10c). These differences affect the spatial extent of grid elements dominated by advective processes (i.e., $Pe > 1$, equation (3)). For example, the convergence associated with $D8$ results in localized upslope expansion of advection-dominated portions of the landscape (Figure 12b) as compared to its extent calculated using a dispersive method like $D8_{\text{frac}}$ (Figure 12c).

The differences in routing are also manifest by the extent of SOF predicted within digital landscapes, which, in some cases, is limited to specific locations that are determined by the flow-routing rule, the slope-calculation rule, and the value of $\frac{T}{q}$ (equation (4), Figure 13). Similar sensitivity to routing rule is apparent when analyzing the extent of landscapes amenable to slope failure (Figure S2). We suspect that MFD-based rules provide more realistic estimates of the distribution of subsurface saturation, and the transition between advective and diffusive processes in landscapes when topographic data are of sufficient resolution to image hillslope portions of the landscape.

4.4. Impact of Flow-Routing and Slope-Calculation Rules on Numerical Models

[43] Interestingly, both qualitative and quantitative properties of topography produced by GTL-based simulations depend on flow-routing and slope-calculation rules. In particular, these rules affect the relief structure of the modeled landscape (Figures 14, S3). The higher relief produced by $D8_{\text{frac}}$, for example, is mainly an outcome of the slope-calculation rule associated with $D8_{\text{frac}}$ (equation (7), Figure S3, Table 2), in which the channel slope is calculated through averaging the slopes to surrounding cells. Such averaging reduces the calculated slope compared to steepest descent and/or facet-based rules. Hence, steady state landscapes produced using $D8_{\text{frac}}$ require the down-facing slopes of each element to increase relative to models that use a steepest descent approach. Thus, the slope averaging produced by $D8_{\text{frac}}$ requires steeper slopes compared to other methods when topographic steepness causes erosion to balance uplift everywhere in the model domain.

[44] We found that the extent of diffusive versus advective processes calculated across a landscape depended, to some degree, on the routing rule chosen in the simulation. For example, the relatively undissected landscape formed by $D4$ and $D8_{\text{frac}}$ (Figure 14), is largely an outcome of the lack of convergence associated with these schemes, either due to the grid imprint ($D4$, Figure 11a), or to the widespread distribution of flow across the landscape ($D8_{\text{frac}}$, Figure 11c). This results in expansion of the diffusive portion of the landscape and in lesser dissection. Because the spacing of channel junctions is dependent on the hillslope extent [*Horton*, 1945; *Perron et al.*, 2009], this relative hillslope expansion is also reflected in the longer channel segments associated with these two schemes (Figure 16). This may also affect segment orientation due to interactions between orientation and length. For example, the surprisingly small number of N-S and E-W oriented segments produced by the $D4$ flow-routing-based models (Figure S5, left column) is likely due to the variety of orientations enabled by longer segments.

[45] The fact that almost every metric we investigated was statistically distinct between simulations (despite identical initial and boundary conditions used in the models, Table 2) suggests that artifacts arising from flow-routing and slope-calculation rules may be imprinted on numerical simulations. While the topographic variations that arise from using different flow-routing and slope-calculation rules may be smaller than errors introduced by the incomplete representation of natural processes by GTLs, these GTLs are currently the primary tool in predicting landscape response to external forcing. As such, it seems prudent to carry out further studies that more fully quantify the impacts of various routing and slope calculation rules. Additionally, modeling studies that seek to compare properties of simulated and real landscapes would benefit from a systematic exploration of the effect of flow-routing and slope-calculation rules on this comparison. We suspect that many landscape metrics may be insensitive to the flow-routing rule used, but the only way to be sure of this is to use multiple simulations that explore the impact of the chosen rule set on the quantities under investigation.

[46] Routing and slope rules may also affect the numerical stability of landscape development models. D_∞, for example, required exceedingly small time steps to maintain the error tolerance we prescribed for the adaptive time step integration [*Dormand and Prince*, 1980; *Press et al.*, 2007]. This likely results from abrupt changes in a cell's drainage area and/or slope that arise when using this rule. These small time steps caused difficulties in achieving a steady state topography in a realistic time frame and forced us to exclude the D_∞ rule from our analysis of modeled landscapes. The computational cost that arises from those is far greater than the cost due to the $n \times 8$ facets used by D_{trig}.

[47] Landscapes simulated using different flow-routing rules should also differ in their response to elevation perturbations (in the context of both *Smith and Bretherton* [1972] and *Perron et al.* [2012]). Flows routed by steepest descent rules such as $D4$, $D8$, and D_∞ are unlikely to be diverted by a perturbation that causes a small slope change relative to the steepest descent slope. In contrast, flows routed by rules that partition flow to all downslope cells, such as $D8_{\text{frac}}$ and D_{trig}, will be diverted by such perturbations. Hence, the sensitivity to perturbations of simulations that use $D8_{\text{frac}}$ and D_{trig}, is higher than that of models using $D4$, $D8$, and D_∞. This conceptual prediction is in accordance with the results of *Pelletier* [2004], where $D8_{\text{frac}}$-based landscape development models do not reach the ideal steady state static topography attained by steepest-descent rules.

4.5. Recommendations

[48] This work indicates that flow-routing rules, in some cases, can importantly impact the results of topographic analyses and numerical simulations of landscape development. Based on these results, we put forth the following recommendations for future studies that attempt to analyze digital topographic data and simulate landscapes using GTL-based rule sets: (A) When calculating specific topographic metrics over real or modeled landscapes, we recommend using a variety of routing rules to compute these metrics to determine their sensitivity to different routing rules. (B) All routing rules contain some element of arbitrariness. As we showed, the properties of a given routing rule may cause it to provide accurate estimates of contributing area and slope in some portions of the landscape, while producing artifactual results in other areas. Additionally, the SFD routing rules likely provide a better representation of channel properties imaged by coarse-resolution DEMs than do the MFD rules. Thus, the appropriate choice of flow-routing rule will depend on the resolution of the topographic data set (or model domain), and the properties of the landscape that one wishes to capture in the analysis or simulation. Comparison of different flow-routing schemes against field survey data may aid in making this choice. (C) Both channel slope and contributing area calculations may depend on the choice of

a flow-routing rule, and so we recommend considering the impact of both when selecting or formulating an appropriate rule.

[49] Second, our results highlight the fact that landscape development models should be constructed in a way that allows easy substitution of flow-routing and slope-calculation rules to examine their impact on simulated topography. We have shown that, at least in DEMs representing real topography, the extent of advective versus diffusive portions of the landscape may depend to some degree on the flow-routing scheme that is selected. Additionally, the extent of SOF and landslides may depend on the rule chosen as well. These choices thus plausibly affect hazard estimations based on topographic data [*Dietrich et al.*, 1992; *Montgomery and Dietrich*, 1994; *Borga et al.*, 1998; *Claessens et al.*, 2005], as well as theoretical studies that, for example, link the extent of advection and diffusion in landscapes to macroscale features of simulated topography [e.g., *Perron et al.*, 2008, 2009, 2012]. One might conjecture that the spatial distribution of these factors may also be impacted by routing and slope rules used to simulate topography given the sensitivity of modeled topographic attributes to these rules.

5. Summary

[50] Flow routing across topography determines drainage area. This study benchmarks common routing rules, as well as a new rule, using a modified, point-source benchmark method that reveals misestimations of SCA that are masked when using standard benchmarks. The new routing rule we propose, D_{trig}, performs comparably to commonly used rules and is advantageous in that it explicitly addresses the internal topography of grid elements and preserves the two-dimensional plan-view geometry of flows. Nonetheless, the grid decomposition associated with this rule may introduce artifacts such as opposing flows. We also explore the effect of routing rules on flow over ALSM-derived topography and show that the choice of a flow-routing rule impacts metrics that predict, for example, the extent of advective versus diffusive processes in a landscape (Péclet number), the extent of SOF, and the extent of shallow landsliding. Finally, we examined the impact of flow-routing rules on modeled topography produced by GTL-based simulations. Analysis of the steady state topography produced by these models shows significant differences in the geometry of the modeled landscapes, and illuminates the role played by both the flow-routing, and slope-calculation rules. Hence, the choice of a flow-routing and/or slope-calculation rule in a landscape analysis and/or modeling study may impact the results, and should be considered in the context of the analysis goals, the resolution of the DEM, and the scale of the geomorphic features of interest. Further studies are necessary to identify morphologic metrics that are most sensitive to these rules and those properties of the landscape that do not strongly record the imprint of the chosen flow-routing rule.

Notation

A drainage area, L^2.
b unit contour length, L.
C_c DEMs cross-correlation value.
D diffusion rate constant, $L^2\ t^{-1}$.
F area fraction routed from a node.
K advection rate constant, $L^{1-2m}\ t^{-1}$.
l channel segment length, L.
m area exponent.
n slope exponent.
N number of downslope elements.
N_t number of nodes in a grid.
N_x number of columns in a grid.
N_y number of rows in a grid.
p slope exponent in the context of *Freeman* [1991].
Pe Péclet number.
q precipitation rate, $L\ t^{-1}$.
r radius, L.
r_o maximal radius, L.
S slope.
S_x slope in x direction.
S_y slope in y direction.
T transmissivity, $L^2\ t^{-1}$.
U uplift, $L\ t^{-1}$.
z elevation, L.
β angle of surface slope.
γ modulus of channel segment orientation divided by 90°, °.
$d\theta$ angular extent of a radial point source.
Δx distance between grid nodes, L.
∇z_c channel slope.
λ Poisson distribution parameter.
ϕ angle of internal friction.

[51] **Acknowledgments.** We would like to thank Alexander Densmore, Nicole Gasparini, Guy Simpson, and an anonymous reviewer for insightful comments that helped in improving this paper. We are also thankful to Sam Johnstone and Seulgi Moon for valuable discussions and early review of this paper, as well as to Erez Tzur and Matan Gavish for providing helpful statistical advice.

References

Band, L. (1986), Topographic partition of watersheds with digital elevation models, *Water Resour. Res.*, *22*(1), 15–24, doi:10.1029/WR022i001p00015.

Borga, M., G. Dalla Fontana, D. Da Ros, and L. Marchi (1998), Shallow landslide hazard assessment using a physically based model and digital elevation data, *Environ. Geol.*, *35*(2), 81–88.

Burrough, P., and R. McDonnell (1998), *Principles of GIS*, 356 pp., Oxford Univ. Press, New York, NY, USA.

Chirico, G., A. Western, R. Grayson, and G. Blöschl (2005), On the definition of the flow width for calculating specific catchment area patterns from gridded elevation data, *Hydrol. Processes*, *19*(13), 2539–2556.

Claessens, L., G. Heuvelink, J. Schoorl, and A. Veldkamp (2005), DEM resolution effects on shallow landslide hazard and soil redistribution modelling, *Earth Surf. Processes Landforms*, *30*(4), 461–477.

Costa-Cabral, M., and S. Burges (1994), Digital elevation model networks (DEMON): A model of flow over hillslopes for computation of contributing and dispersal areas, *Water Resour. Res.*, *30*(6), 1681–1692, doi:10.1029/93WR03512.

Culling, W. (1960), Analytical theory of erosion, *J. Geol.*, *68*(3), 336–344.

Culling, W. (1963), Soil creep and the development of hillside slopes, *J. Geol.*, *71*(2), 127–161.

Culling, W. (1965), Theory of erosion on soil-covered slopes, *J. Geol.*, *73*(2), 230–254.

DeLong, S. B., C. S. Prentice, G. E. Hilley, and Y. Ebert (2012), Multitemporal ALSM change detection, sediment delivery, and process mapping at an active earthflow, *Earth Surf. Processes Landforms*, *37*(3), 262–272.

Dietrich, W., C. Wilson, D. Montgomery, J. McKean, and R. Bauer (1992), Erosion thresholds and land surface morphology, *Geology*, *20*(8), 675–679.

Dietrich, W., C. Wilson, D. Montgomery, and J. McKean (1993), Analysis of erosion thresholds, channel networks, and landscape morphology using a digital terrain model, *J. Geol.*, *101*, 259–278.

Dietrich, W. E., D. G. Bellugi, L. S. Sklar, J. D. Stock, A. M. Heimsath, and J. J. Roering (2003), Geomorphic transport laws for predicting landscape form and dynamics, in *Geophysical Monograph Series,* vol. 135, edited by P. Wilcock and R. Iverson, pp. 103–132, AGU, Washington, D. C., doi:10.1029/135GM09.

Dormand, J., and P. Prince (1980), A family of embedded Runge-Kutta formulae, *J. Comput. Appl. Math.*, *6*(1), 19–26.

Fairfield, J., and P. Leymarie (1991), Drainage networks from grid digital elevation models, *Water Resour. Res.*, *27*(5), 709–717, doi:10.1029/90WR02658.

Freeman, T. (1991), Calculating catchment area with divergent flow based on a regular grid, *Comput. Geosci.*, *17*(3), 413–422.

Horton, R. (1945), Erosional development of streams and their drainage basins; Hydrophysical approach to quantitative morphology, *Geol. Soc. Am. Bull.*, *56*(3), 275–370.

Howard, A., and G. Kerby (1983), Channel changes in badlands, *Geol. Soc. Am. Bull.*, *94*(6), 739–752.

Howard, A. D. (1994), A detachment-limited model of drainage basin evolution, *Water Resour. Res.*, *30*(7), 2261–2286, doi:10.1029/94WR00757.

Kruskal, W., and W. Wallis (1952), Use of ranks in one-criterion variance analysis, *J. Am. Stat. Assoc.*, *47*(260), 583–621.

Lea, N. L. (1992), An aspect driven kinematic routing algorithm, in *Overland Flow: Hydraulics and Erosion Mechanics*, edited by A. J. Parsons and A. D. Abrahams, pp. 393–407, Chapman and Hall, New York.

Mackey, B. H., and J. J. Roering (2011), Sediment yield, spatial characteristics, and the long-term evolution of active earthflows determined from airborne lidar and historical aerial photographs, Eel River, California, *Geol. Soc. Am. Bull.*, *123*(7-8), 1560–1576.

McCormack, J., M. Gahegan, S. Roberts, J. Hogg, and B. Hoyle (1993), Feature-based derivation of drainage networks, *Int. J. Geogr. Inf. Syst.*, *7*(3), 263–279.

Montgomery, D., and W. Dietrich (1994), A physically based model for the topographic control on shallow landsliding, *Water Resour. Res.*, *30*(4), 1153–1171, doi:10.1029/93WR02979.

Moore, I., and R. Grayson (1991), Terrain-based catchment partitioning and runoff prediction using vector elevation data, *Water Resour. Res.*, *27*(6), 1177–1191, doi:10.1029/91WR00090.

O'Callaghan, J., and D. Mark (1984), The extraction of drainage networks from digital elevation data, *Comput. Vision Graph. Image Process.*, *28*(3), 323–344.

Orlandini, S., and G. Moretti (2009), Determination of surface flow paths from gridded elevation data, *Water Resour. Res.*, *45*, W03417, doi:10.1029/2008WR007099.

Orlandini, S., G. Moretti, M. Franchini, B. Aldighieri, and B. Testa (2003), Path-based methods for the determination of nondispersive drainage directions in grid-based digital elevation models, *Water Resour. Res.*, *39*(6), 1144, doi:10.1029/2002WR001639.

Passalacqua, P., T. Do Trung, E. Foufoula-Georgiou, G. Sapiro, and W. E. Dietrich (2010), A geometric framework for channel network extraction from lidar: Nonlinear diffusion and geodesic paths, *J. Geophys. Res.*, *115*, F01002, doi:10.1029/2009JF001254.

Pelletier, J. (2004), Persistent drainage migration in a numerical landscape evolution model, *Geophys. Res. Lett.*, *31*, L2050, doi:10.1029/2004GL020802.

Perron, J., W. Dietrich, and J. Kirchner (2008), Controls on the spacing of first-order valleys, *J. Geophys. Res.*, *113*, F04016, doi:10.1029/2007JF000977.

Perron, J., J. Kirchner, and W. Dietrich (2009), Formation of evenly spaced ridges and valleys, *Nature*, *460*(7254), 502–505.

Perron, J., P. Richardson, K. Ferrier, and M. Lapôtre (2012), The root of branching river networks, *Nature*, *492*(7427), 100–103.

Press, W., S. Teukolsky, W. Vetterling, and B. Flannery (2007), *Numerical Recipes: The Art of Scientific Computing, 3rd edn. Cambridge, NY*, 1256 pp., University Press, USA.

Qin, C., A. Zhu, T. Pei, B. Li, C. Zhou, and L. Yang (2007), An adaptive approach to selecting a flow-partition exponent for a multiple-flow-direction algorithm, *Int. J. Geogr. Inf. Sci.*, *21*(4), 443–458.

Quinn, P., K. Beven, P. Chevallier, and O. Planchon (1991), The prediction of hillslope flow paths for distributed hydrological modelling using digital terrain models, *Hydrol. Processes*, *5*(1), 59–79.

Refsgaard, J. (1997), Parameterisation, calibration and validation of distributed hydrological models, *J. Hydrol.*, *198*(1-4), 69–97.

Seidl, M., and W. Dietrich (1992), The problem of channel erosion into bedrock, in *Functional Geomorphology: Landform Analysis and Models: Festschrift for Frank Ahnert,* vol. Catena Supplement 23, edited by K. Schmidt and J. de Ploey, pp. 101–124, Cremlingen, Germany, Catena Verlag.

Smith, T. R., and F. P. Bretherton (1972), Stability and the conservation of mass in drainage basin evolution, *Water Resour. Res.*, *8*(6), 1506–1529, doi:10.1029/WR008i006p01506.

Tarboton, D. (1997), A new method for the determination of flow directions and upslope areas in grid digital elevation models, *Water Resour. Res.*, *33*, 309–319, doi:10.1029/96WR03137.

Tucker, G., and R. Bras (1998), Hillslope processes, drainage density, and landscape morphology, *Water Resour. Res.*, *34*(10), 2751–2764, doi:10.1029/98WR01474.

Tucker, G., and G. Hancock (2010), Modelling landscape evolution, *Earth Surf. Processes Landforms*, *35*(1), 28–50.

Whipple, K., and G. Tucker (1999), Dynamics of the stream-power river incision model: Implications for height limits of mountain ranges, landscape response timescales, and research needs, *J. Geophys. Res.*, *104*, 17,661–17,674, doi:10.1029/1999JB900120.

Wolock, D., and G. McCabe Jr (1995), Comparison of single and multiple flow direction algorithms for computing topographic parameters in TOPMODEL, *Water Resour. Res.*, *31*(5), 1315–1324, doi:10.1029/95WR00471.

Zhang, W., and D. Montgomery (1994), Digital elevation model grid size, landscape representation, *Water Resour. Res.*, *30*(4), 1019–1028, doi:10.1029/93WR03553.

Zhou, Q., and X. Liu (2002), Error assessment of grid-based flow-routing algorithms used in hydrological models, *Int. J. Geogr. Inf. Sci.*, *16*(8), 819–842.